Diverse mixing state and ice nucleation properties of aerosol particles over the Western Pacific and the Southern Ocean

Jiao Xue[1], Tian Zhang[1], Keyhong Park[2], Jinpei Yan[3], Young Jun Yoon[2], Jiyeon Park[2,*], Bingbing Wang[1,4,*]

[1] State Key Laboratory of Marine Environmental Science, College of Ocean and Earth Sciences, Xiamen University, Xiamen, 361102 China

[2] Korea Polar Research Institute, Incheon, 21990 South Korea

[3] Third Institute of Oceanography, Ministry of Natural Resources, Xiamen 361005, China

[4] Center for Marine Meteorology and Climate Change, Xiamen University, Xiamen, 361102 China

Correspondence: Bingbing Wang (Bingbing.Wang@xmu.edu.cn) and Jiyeon Park (jypark@kopri.re.kr).

Abstract

Atmospheric particles can impact cloud formation and play a critical role in regulating cloud properties. However, particle characteristics at the single particle level and their ability to act as ice nucleating particles (INPs) over the marine atmosphere are poorly understood. In this study, we present micro-spectroscopic characterizations and ice nucleation properties of particles collected during a cruise from South Korea to Antarctica in 2019. Most of the samples were dominated by fresh sea salt, aged sea salt, and sea salt mixed with sulfate particles, with total number percentages ranging from 48% to 99% over the Western Pacific and the Southern Ocean. The mixing state index of the particle population ranged from 50% to 95% over the northern and southern hemispheres. Multiphase processes on sea salt particles resulted in chlorine deficiency. This selective aging process made the marine particle population more externally mixed. Ice nucleation onset conditions were measured and the investigated particles showed diverse ice nucleation abilities. The fresh sea salt particles with organic coatings exhibited the highest ice nucleation ability at a relative humidity with respect to ice as low as 121%. The sea salt mixed sulfate particle was enriched in INPs by a factor of 1.9. Aging processes affected both particles' mixing state and their ice nucleation abilities. Our analysis shows that assuming an internally mixed particle population in the marine atmosphere can lead to errors of several orders of magnitude in predicting ice nucleation rates.

Keywords: Ice nucleation, ice nucleating particles, single particle analysis, marine aerosols, elemental composition, mixing state

1. Introduction

As 70.8% of the Earth's surface is covered by oceans, marine aerosol particles are one of the most important types of natural aerosols in the global inventory (Myriokefalitakis et al., 2010; De Leeuw et al., 2011). Aerosols in marine environments can affect the ocean biogeochemical cycles and indirectly or directly affect Earth system's radiation budget (Song et al., 2022). The sixth Intergovernmental Panel on Climate Change (IPCC) assessment report highlights a significant uncertainty in predicting the net effective radiative forcing of aerosols, with aerosol-cloud interactions contribute the most (IPCC, 2021). The impacts of atmospheric particles on cloud microphysical processes are still poorly understood (IPCC, 2013). The physicochemical properties of particles determine their abilities to serve as cloud condensation nuclei (CCN) and INPs, thereby affecting cloud microphysical processes. Particles serving as INPs can potentially trigger ice nucleation via four pathways: (1) deposition ice nucleation (DIN), which forms ice by the direct deposition of water vapor onto particle surface; (2) immersion freezing (IMF), which droplet freezing is triggered by immersed particles; (3) contact freezing, when droplets freeze by the contact with particles; (4) condensation freezing, when droplets freeze as water vapor condenses on droplets or particles. The majority of recent studies have focused on the IMF and DIN under mixed-phase and ice cloud conditions (Hoose and Möhler, 2012; Murray et al., 2012; Kanji et al., 2017; Knopf et al., 2018).

Diverse sources and atmospheric processes bring great challenges to the study of the physicochemical properties of marine particles. One of the major particle types in the marine atmosphere is sea spray aerosol (SSA) generated from wave breaking and bubble bursting over the ocean surface. Their compositions are mainly affected by seawater, sea ice, and biological activities and have minimum influence from anthropogenic activities (Kunwar et al., 2023). Other sources may also contribute to marine aerosols, such as ship emission (Ault et al., 2009, 2010) and long-range transport of aerosols from industrial emission, biomass burning, dust storms, and fossil fuel

71 combustion (Han et al., 2006; Fu et al., 2013; Geng et al., 2019). In addition,

72 atmospheric oxidation of volatile organic compounds from the ocean or anthropogenic

73 activities results in gas-particle conversion, multiphase reactions, and the formation of

74 secondary materials on particles (Cochran et al., 2017). For example, dimethyl sulfide

75 (DMS) from marine sources can be oxidized to form methanesulfonic acid (MSA) and

76 sulfuric acid (H_2SO_4) in the atmosphere (Barnes et al., 2006; Chen et al., 2018; Berndt

77 et al., 2023). Moreover, multiphase reactions can occur on the surface or within particles

78 causing changes in the physicochemical properties of particles (Cochran et al., 2017).

79 The oxidation products of DMS (H_2SO_4 and MSA) can react with sea salt particles

80 resulting in chloride depletion from acid displacements (Liu et al., 2011).

81

82 Due to the diverse sources and dynamic evolution in the atmosphere, individual

83 particles become mixtures of various compositions and have complex morphologies.

84 Chemical mixing state is a term used to describe how various chemical species are

85 mixed within individual particles in an aerosol population (Riemer et al., 2019). Riemer

86 and West (2013) proposed a framework to quantify the chemical mixing state, which is

87 described later in Section 2.3. Quantifying the chemical mixing state helps us to discuss

88 how the population with different internal or external mixing affects its optical

89 properties, cloud formation properties, and climatic impacts (Riemer et al., 2019). It is

90 necessary to study the physical and chemical characteristics of individual particles as

91 well as how they are mixed in the population to quantify the fundamental details of

92 cloud microphysical processes (Cziczo et al., 2017; Kanji et al., 2017; Knopf et al.,

93 2018; Riemer et al., 2019; Burrows et al., 2022). Using single-particle techniques,

94 previous studies have focused on mixing states including but not limited to marine

95 particles (Ault et al., 2010; Park et al., 2014; Tomlin et al., 2021), biomass burning

96 aerosol (BBA) (Tomlin et al., 2022; Healy et al., 2013), and dust particles (Fraund et

97 al., 2017; Adachi et al., 2020). Previous studies have quantified the chemical mixing

98 state of an aerosol population using the mixing state index (χ), which is based on the

99 mass percentages of various chemical species in single particles within a population

100 (Riemer et al., 2019). However, there have been limited studies focusing on quantifying

101   χ from single particle component information of marine particles.

102

103   Laboratory and field studies have shown that various particle types have potential

104   impacts on atmospheric ice crystal formation. Natural INPs include mineral dust, soil

105   particles, volcanic ash, SSA, BBA, and bioaerosols. Anthropogenic INPs include

106   agricultural particles, metals and metal oxides from industrial processes, and fossil fuel

107   combustion particles (Hoose and Möhler, 2012; Murray et al., 2012; Kanji et al., 2017).

108   For marine related particles, Schill and Tolbert (2014) found that SSA are efficient INPs

109   below 225 K. Wagner et al. (2018) showed that SSA and desert dust particles share the

110   same order of magnitude of ice nucleation active surface site density (n_s) for deposition

111   nucleation. Previous studies have also shown that n_s for SSA is 2-3 orders of magnitude

112   lower than that for dust particles in immersion freezing (DeMott et al., 2016;

113   McCluskey et al., 2018a; Cornwell et al., 2019). Knopf et al. (2011) confirmed that

114   intact cells or fragments of marine diatoms can act as INPs. Wilson et al. (2015)

115   demonstrated that the sea surface microlayer is enriched with ice nucleating materials.

116   McCluskey et al. (2018b) identified two types of INPs from mesocosm experiments,

117   which were dissolved organic carbon coated particles and particulate organic carbon

118   particles like intact cells or cell fragments from microorganisms. Alpert et al. (2022)

119   confirmed that INPs in the SSA were the sea salt with organic matter, which were

120   exudates released from planktonic microorganisms. Inoue et al. (2021) found high INP

121   concentrations under high wave conditions which were related to the release of organic

122   carbon from the ocean. Welti et al. (2020) collected the INP concentration data over the

123   Arctic, Atlantic, Pacific, and Southern oceans. They found that ship-based INP

124   measurements over the oceans were 1 to 2 orders of magnitude lower than continental

125   observations. INP concentrations were lowest in the polar regions and highest in the

126   temperate climate ocean (Welti et al., 2020). Most of the field investigations over

127   oceans focus on the INP concentration measurements for IMF and at mixed-phase cloud

128   conditions with relatively warmer temperatures (Hoose and Möhler, 2012; Murray et

129   al., 2012; Kanji et al., 2017; Knopf et al., 2018). Recent field studies have used

130   advanced micro-spectroscopes and mass spectrometry to image and characterize the

INPs and ice crystal residuals to understand their nature (e.g., Cziczo et al., 2017; Knopf et al., 2018). INPs and ice residuals are often mixtures of chemical species. Ice nucleation is inherently related to the mixing state of particles because it depends on the particle surface properties. Quantifying the ice nucleation rate also depends on the details of composition, surface area, and the mixing state of the particle population. The importance of mixing state for INPs is well recognized, but there are limited studies focusing on its quantification which is poorly understood (Kanji et al., 2017; Knopf et al., 2018; Riemer et al., 2019).

In this study, we quantified ice formation potential and elemental composition of particles over coastal and open oceans using microscope-based ice nucleation instrumentation and computer-controlled scanning electron microscopy with energy dispersive X-ray spectroscopy (CCSEM/EDX), respectively. The mixing state of particle population based on the elemental composition was derived for 29 marine ambient particle populations extending from the northern to the southern hemisphere. Ice nucleation onset conditions were measured and the INPs were identified for representative samples. Individual INPs were characterized and compared with the particle population to relate ice nucleation ability to the mixing state. Potential errors in predicting ice nucleation rate were briefly discussed if models assume an internally mixed population. We performed ice nucleation kinetic analysis based on the experimental data and provided parameterizations for cloud modeling.

2. Experimental methods

2.1 Particle sampling

Aerosol particles were collected by a four-stage cascade impactor (SKC, Inc.) at a sample flow of 9 L min^{-1} on board the Korean ice breaker R/V *Araon* from October 31st to December 12nd in 2019. Particles were collected on the third and fourth stages of the impactor with 50% collection efficiency at aerodynamic sizes of 0.5 μm and 0.25 μm, respectively. The inlet was located on the third deck of the ship at about 13 m above sea

surface level (Park et al., 2020). As shown in Fig. 1, the cruise crossed about 110

degrees of latitude from the Western Pacific near South Korea (34.93°N) to the Ross

Sea in the Southern Ocean (75.12°S). Samples were collected on transmission electron

microscopy (TEM) copper grids (Carbon Type-B, Ted Pella, Inc.) for single particle

analysis by CCSEM/EDX and silicon wafer chips (Silson, Ltd.) with the hydrophobic

coating (Si_3N_4) for ice nucleation experiments following our previous studies (Wang et

al., 2012a, 2016a; Knopf et al., 2014). Particles were collected simultaneously on these

two substrates which were placed side by side in the same impactor. Particle samples

were stored at room temperature in an airtight container with desiccant until analysis.

This study focuses on deposition ice nucleation at low temperatures and INP

identification. Particles with a smaller size range may have a longer lifetime and can

potentially be transported to higher altitudes in the atmosphere. Therefore, we limited

our analysis to the samples collected on the fourth stage. Meteorological conditions and

black carbon concentrations were measured by the onboard weather station and an

aethalometer (AE22, Magee Scientific Co., USA), respectively. When the relative wind

direction against the ship heading is between 110° and 260° and the relative wind speed

is below 2 m s^{-1}, samples may have been influenced by the ship exhaust (Park et al.,

2020). Potentially contaminated samples were excluded from the analysis, resulting in

a total of 29 selected samples. The sampling location and 72 h backward air mass

trajectories are shown in Fig. 1. Backward air mass trajectories were computed using

the Hybrid Single-Particle Lagrangian Integrated Trajectory (HYSPLIT) model (Stein

et al., 2015; Rolph et al., 2017). Detailed sampling information is listed in Table S1 and

includes the collecting time, location, and the corresponding meteorological data. Black

carbon concentration, air temperature, relative humidity, pressure, relative wind speed,

and wind direction are also shown in Fig. S1.
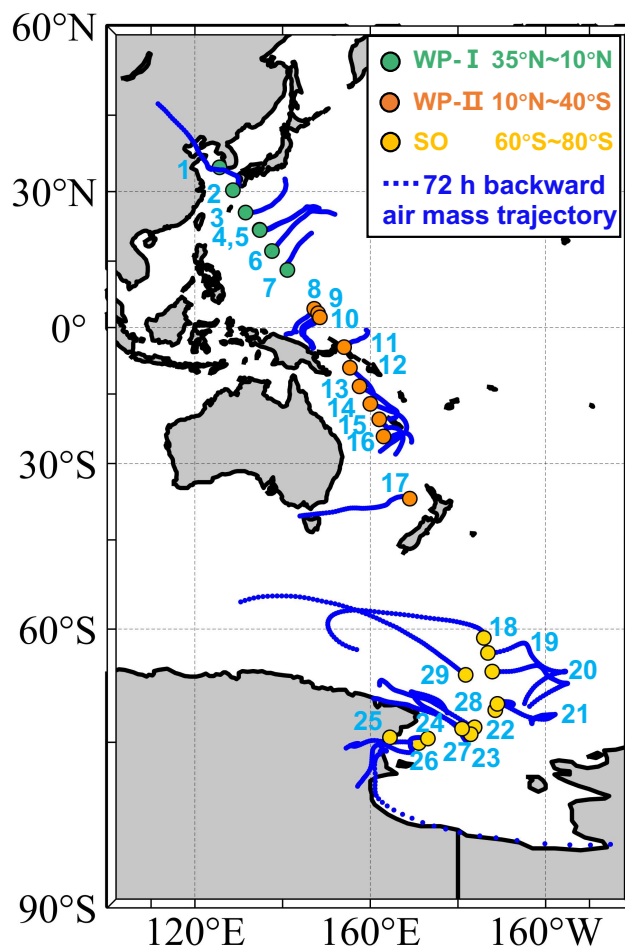
Figure 1. Sampling locations with HYSPLIT 72 h backward air mass trajectories. Solid circles indicate the sample locations. Samples were labeled by numbers. Green, orange, and yellow circles represent the samples in 35°N − 10°N of Western Pacific (WP-I), 10°N − 40°S of Western Pacific (WP-II), and 60°S − 80°S of Southern Ocean (SO) regions, respectively. Blue lines show the backward trajectories starting from 100 m above sea level.

2.2 Chemical imaging and characterization of particles and INPs

Chemical imaging and single particle analysis were used to obtain information on the morphology, size, and elemental composition of the particle population and INPs. The methods have been described in detail in previous work (Laskin et al., 2002, 2006, 2012; Wang et al., 2012a; Knopf et al., 2014; O'Brien et al., 2015) and are briefly introduced here. Samples collected on the TEM grids were analyzed using a scanning electron microscopy (Quanta 650, FEI Inc.) equipped with an energy dispersive X-ray

spectroscopy (Genesis, EDAX Inc.) in the computer-controlled mode (CCSEM/EDX). CCSEM/EDX operating at 20 kV first detected the particles and determined their size. The particle size reported here is the equivalent circle diameter (ECD) based on the two-dimensional projected area of the particle as determined by CCSEM/EDX analysis. Particles with a size (ECD) between 0.2 μm and 3 μm were included for analysis in this study. The elemental composition of each particle was then quantified by determining the relative atomic percentages of the selected elements, including C, N, O, Na, Mg, Al, Si, P, S, Cl, K, Ca, Mn, and Fe. We obtained the elemental composition for a significant number of particles, about 630 – 1480 particles for each sample depending on the particle loading on the substrates (Table S1). We manually performed SEM/EDX analysis to characterize the individual identified INPs on the silicon wafer chips after ice nucleation experiments, as described later. In addition, about 10 particles that did not nucleate ice (non-INPs) were randomly selected around each INP for SEM/EDX analysis. X-ray spectra for the INPs and non-INPs were collected at 10 kV. The relative atomic percentages of elements including C, O, Na, Mg, Al, P, S, Cl, K, and Ca were quantified. N and Si were not included in the quantification due to their presence in the background substrate.

The relative atomic percentage data were analyzed using a rule-based classification method to assess the contributions of different particle types for each sample (Laskin et al., 2012; Wang et al., 2012a; China et al., 2018; Lata et al., 2021). As shown in Fig. 2, the classification scheme grouped particles into seven classes: *i*) "CNO" particles, which mainly contain C, N, and O elements with traces of other elements. These are carbonaceous particles such as black carbon, secondary or primary organic particles. *ii*) "CNOS" particles, which mainly contain C, N, O, and S elements with traces of other elements and are sulfates and other sulfur containing particles including their internal mixtures with organics. *iii*) "FreshSS" particles, these are fresh sea salt particles containing Na above a threshold level of 2% (atomic percentage) and the Cl/Na ratio is > 0.8. At the same time, the total atomic percentage of Na, Mg, and Ca, which are the dominant cations in sea salt particles, is higher than that of other metals. CCSEM/EDX

229 analysis of fresh sea salt particles generated by nebulizing sea water shows that the

230 Cl/Na ratio is slightly higher than 0.8 for particles at about 0.2 μm (Fig. S2). The

231 samples we investigated contain a large number of small sea salt particles. Thus, we

232 use a Cl/Na ratio of 0.8 as the threshold value to distinguish between the fresh and aged

233 sea salt particles. *iv*) "AgedSS" particles, these are aged sea salt particles with Cl

234 depletion and the Cl/Na ratio < 0.8. *v*) "SS/Sulf" particles, these are aged sea salt

235 particles mixed with sulfur-containing compounds (e.g., sulfate) containing mainly Na

236 and S without Cl. *vi*) "Dust" particles, these particles have the total atomic percentage

237 of Al and Si above 4% and higher than the total atomic percentage of Na and Mg. They

238 are likely from dust storms and road or soil emissions. *vii*) "Mixture" particles are all

239 remaining particles that did not fit into the previous categories. The classification

240 scheme for INPs and non-INPs on silicon wafer chips was modified to account for the

241 Si and N background in the substrate. It is important to note that particles on either

242 TEM grids or Si chips were collected at the same time using the same impactor, and

243 therefore the contributions of the respective particle classes for the two are the same.

244 Thus, we modified the classification scheme with this assumption.

245
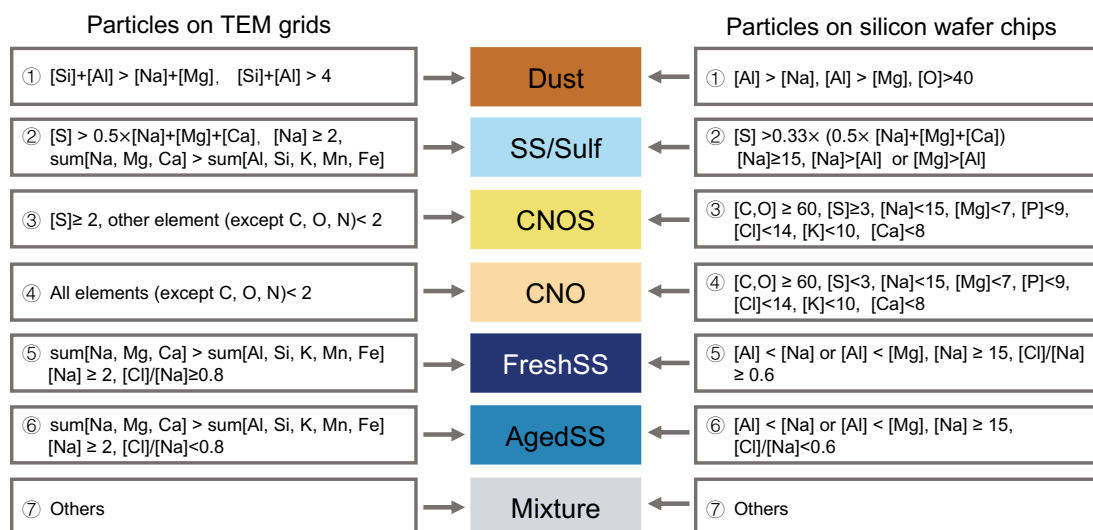
246

247 **Figure 2.** Rule-based particle classification schemes for particles on TEM grids (left) and silicon

248 wafer chips (right). Numbers in the schemes are the relative atomic percentages of corresponding

249 elements or their ratios.

2.3 Chemical mixing state

Chemical mixing state was derived using a previous methodology based on mass and entropy metrics (O'Brien et al., 2015; Riemer and West, 2013) and is described briefly here. Particle mass was estimated from the density and volume of each particle. Particles were assumed to be hemispherical and the volume of each particle was calculated from the ECD obtained by CCSEM. Particle density was assigned according to its classification, with FreshSS, AgedSS, SS/Sulf, CNO, CNOS, Dust, and Mixture particles having a density of 2.0 g/cm^3, 2.0 g/cm^3, 1.7 g/cm^3, 1.3 g/cm^3, 1.3 g/cm^3, 2.7 g/cm^3, and 2.0 g/cm^3, respectively (O'Brien et al., 2015; Tang et al., 2014). To calculate the mass of each element in a particle, the atomic percentage of each element obtained by EDX was converted to a weight percentage, and then multiplied by the mass of the particle. For the particle i, the mass of element a is equal to:

$$\mu_i^a = \mu_i \left(\frac{elemental\%^a \times molar\ mass^a}{\sum_{a=1}^{A} elemental\%^a \times molar\ mass^a} \right) \tag{1}$$

Where $a = 1, \ldots, A$ (number of elements), $i = 1, \ldots, N$ (number of particles), and μ_i is the total mass of the ith particle. a represents elements of Na, Mg, Al, Si, P, S, Cl, K, Ca, Mn, and Fe, and for this list, $A = 11$. Note that C, N, and O are not included as these three elements are semi-quantitative when EDX analysis is used (Laskin et al., 2006).

First, the total mass of element a in the particle population (μ^a), and the total mass of the bulk particle population (μ) were calculated using the following equations,

$$\mu^a = \sum_{i=1}^{N} \mu_i^a \ , \tag{2}$$

and

$$\mu = \sum_{i=1}^{N} \mu_i \ . \tag{3}$$

Then, the mass fraction of element a in the ith particle (p_i^a), the mass fraction of individual particles (p^i) in the particle population, and the mass fraction of element a in the bulk particle population (p^a) are

277 $$p_i^a = \frac{\mu_i^a}{\mu_i},$$ (4)

278 $$p_i = \frac{\mu_i}{\mu},$$ (5)

279 and

280 $$p^a = \frac{\mu^a}{\mu}.$$ (6)

281 Next, the following Shannon entropies (MacKay, 2003) were calculated, where the

282 mixing entropy of the ith particle (H_i) is

283 $$H_i = \sum_{a=1}^{A} -p_i^a \, lnp_i^a,$$ (7)

284 the average particle mixing entropy (H_a) is

285 $$H_a = \sum_{i=1}^{N} p_i H_i,$$ (8)

286 and the mass entropy of bulk particle population (H_γ) is

287 $$H_\gamma = \sum_{a=1}^{A} -p^a lnp^a.$$ (9)

288 H_i and H_γ are used to describe the mass distribution of species (elements) with the ith

289 particle or particle population, respectively. A higher entropy indicates a more uniform

290 distribution of elements in the individual particle or particle population whereas a lower

291 entropy towards a non-uniform mass distribution.

292

293 Individual particle diversity (D_i) is calculated by taking the exponent of H_i. D_i means

294 the effective number of elements in individual particles, or in other words, indicates the

295 distribution of elements in single particles. D_i ranges from the minimum value of 1

296 when the particle contains a single element to the maximum value of A when the particle

297 is composed of all A elements with equal mass. Particle elemental diversity (D_a) and

298 bulk population elemental diversity (D_γ) are calculated by taking the exponent of H_a

299 and H_γ, respectively. D_a indicates the average effective number of elements in particles.

300 D_γ indicates the effective number of elements in the whole particle sample.

301
$$D_i = e^{H_i} = \prod_{a=1}^{A} (p_i^a)^{-p_i^a} \qquad (10)$$

302
$$D_\alpha = e^{H_\alpha} = \prod_{i=1}^{N} (D_i)^{p_i} \qquad (11)$$

303
$$D_\gamma = e^{H_\gamma} = \prod_{a=1}^{A} (p^a)^{-p^a} \qquad (12)$$

304 Mixing state index (χ) indicates the homogeneity or heterogeneity of the population and
305 is defined as

306
$$\chi = \frac{D_\alpha - 1}{D_\gamma - 1} . \qquad (13)$$

307 χ ranges from 0% for an externally mixed particle sample with a heterogeneous
308 population composing single-component particles ($D_\alpha = 1$) to 100% for an internally
309 well mixed particle sample with a homogeneous population where all particles have
310 identical compositions.

311

312 **2.4 Ice nucleation experiment and INP identification**
313 Ice nucleation and water uptake by particles were examined following our previous
314 studies (Knopf et al., 2011, 2014, 2022; Wang and Knopf, 2011; Wang et al., 2012b;
315 Charnawskas et al., 2017; China et al., 2017; Alpert et al., 2022) and the methods are
316 briefly introduced here. Onset conditions of the particle temperature (T_p) and relative
317 humidity with respect to ice (RH_{ice}), when ice nucleation and water uptake occurred,
318 were determined using a custom-built cryo-cooling system. The system consists of a
319 water vapor control component, an ice nucleation cell (INC), and an optical microscope
320 (OM). Prior to ice nucleation experiments, a particle sample collected on a silicon wafer
321 was placed in the INC. Then, a humidified N_2 gas with targeted water vapor partial
322 pressure was continuously introduced into INC at a flow rate of one standard liter per
323 minute. The water partial pressure in the INC was determined by the dew point
324 temperature (T_d) of the gas which was measured using a chilled mirror hygrometer (GE
325 Sensing, Optica). After T_d was stable, T_p was set to about $T_d + 3$ K and $RH_{ice} < 100\%$.
326 An ice nucleation experiment was started and T_p was cooled at a rate of 0.2 K min^{-1}.

Images of particle sample were recorded by OM every 0.02 K. T_d and T_p were recorded every second throughout the experiment. Once ice formation was observed, the sample was gradually warmed to 298 K to sublime and remove any ice that may be retained in the pores or cavities of particles. Images of ice crystals were acquired during sublimation at high magnification and the visible particle that served as the INP was identified after complete crystal sublimation. The experiment was repeated 3 – 7 times at similar T_d for reproducibility. Water uptake and ice formation by particles were determined through visual observation and the changes in particle phase or size from analyzing the recorded images using ImageJ software. through visual observation. DIN and IMF were discriminated based on whether particles took up water before ice formation. The freezing mechanism within the small droplets after the water uptake could not be visualized due to the limited spatial resolution and imaging speed of the OM used in this study. Thus, we assume that immersion freezing has occurred if the RH_{ice} onset of freezing is lower than the homogeneous freezing limits. Only the temperature and RH_{ice} conditions when the first ice crystal formed were reported. RH_{ice} was derived from the measured T_d and T_p (Wang and Knopf, 2011). Particle surface area available for ice nucleation for each sample was estimated from the particle number and size derived from OM images, assuming that the particles were hemispheres. The conservative uncertainty of a factor of 2 for particle surface area was estimated using the standard deviation of the means with assumption of particles being flat or spherical. This assumption likely underestimates the actual surface area since most of the particles deposited on the substrate exhibited non-spherical geometry and may have had rough surfaces including cracks or cavities. The particle surface areas were later used for ice nucleation kinetic analysis. INPs were identified using the recorded optical images during ice nucleation, ice growth, and ice sublimation. Using these optical images, INPs were relocated in the SEM using digital pattern recognition and triangulation and then were imaged and analyzed by SEM/EDX (Knopf et al., 2014).

The temperature and water vapor distribution within the INC were calibrated and validated following our previous work (Wang and Knopf, 2011; Wang et al., 2016b).

357 Homogeneous water vapor distribution in the INC was confirmed by uniform

358 condensation and evaporation of micro-meter size water droplets across the 0.5 mm^2

359 sample area. T_p was calibrated by the melting points of ice, dodecane, decane, octane,

360 and heptane. The calibration confirmed that the response of T_p is linear in the range of

361 180 – 273 K with an uncertainty less than 0.3 K. Conservative uncertainty in RH_{ice} for

362 this experimental system comes from the uncertainty in T_d and T_p ($\Delta T_d < \pm 0.15$ K and

363 $\Delta T_p < \pm 0.3$ K), resulting in $\Delta RH_{ice} < \pm 11\%$ at 200 K and $\Delta RH_{ice} < \pm 3\%$ at 260 K.

364

3. Results and discussion

3.1 Particle characterization

367 Figure 3 shows the typical SEM images and the corresponding EDX spectra of the

368 identified particle classes. FreshSS and AgedSS particles were dominated by Na with

369 different contents of Cl. The FreshSS particle exhibited a cubic NaCl crystal

370 morphology (black solid square) with irregular materials (bright coating) under the

371 transmission detector of SEM at darkfield mode. The coating likely comprised other

372 materials in seawater including MgSO$_4$ and CaSO$_4$ (Xiao et al., 2008). The AgedSS

373 particle showed a non-cubic shape NaCl crystal shape as its core surrounded by

374 substances containing Na with depletion of Cl. The depletion of Cl indicates that the

375 particle had been aged, possibly due to the formation of gaseous HCl by chemical

376 reactions with nitric acid, sulfuric acid, and organic acids in the atmosphere (Laskin et

377 al., 2012; Wang et al., 2015; Angle et al., 2021; Su et al., 2022). The SS/Sulf particle

378 showed in Fig. 3 had a core-shell structure and was mainly composed of Na and S

379 without Cl. This suggests that it was a completely aged sea salt particle coated with

380 sulfur-containing components, such as sulfate. The CNOS and CNO particles showed

381 a round-shaped morphology. The Dust-like particle exhibited clear Al and Si peaks with

382 minor Ca. Figure 4 shows the particle classification results of over 30,000 particles in

383 29 samples investigated by CCSEM/EDX. The size-resolved chemical distributions for

384 all samples are shown in Fig. S3, with FreshSS and AgedSS particles dominating all

385 size bins. The majority of SS/Sulf particles were larger than 0.5 μm, while the CNOS

386 and CNO particles were mainly in the sub-micrometer size range. As shown in Fig. 1

387 and Fig. 4, the samples (S1 – S29) were separated into the following three regions

388 according to the latitudes of the sampling locations, 35°N – 10°N of the Western Pacific

389 (WP-I), 10°N – 40°S of the Western Pacific (WP-II), and 60°S – 80°S of the Southern

390 Ocean (SO).

391

392
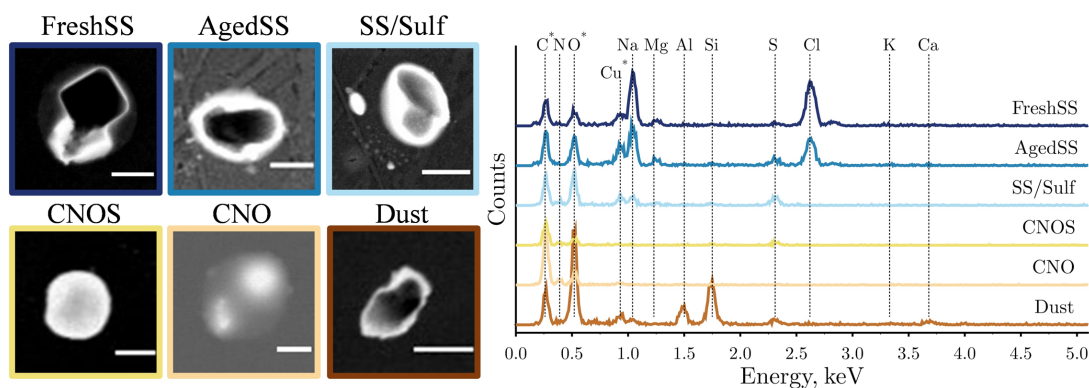
Figure 3. Representative SEM images and the corresponding EDX spectra for particles from each class. The peaks in spectra for the C, O, and Cu elements (asterisked) may include some signal from substrate background of TEM grids. SEM images were captured at 20 kV using scanning transmission electron microscopy detector. The scale bar for all images is 1 μm.

397

398 Figure 4 shows that in the WP-I region (35°N – 10°N, S1 – S7), the proportion of

399 FreshSS and AgedSS particles increased from 10% to 91% as the ship moved away

400 from the land, indicating an increased contribution of SSA. The contribution of the Dust

401 particle class decreased from 59% to 8% for S1 to S3. The Navy Aerosol Analysis and

402 Prediction System reanalysis (NAAPS-RA) product indicated a dust storm during the

403 S1 and S2 sampling periods (Fig. S4). The 72 h backward air mass trajectories also

404 showed that the air mass passed through areas affected by the dust storm.
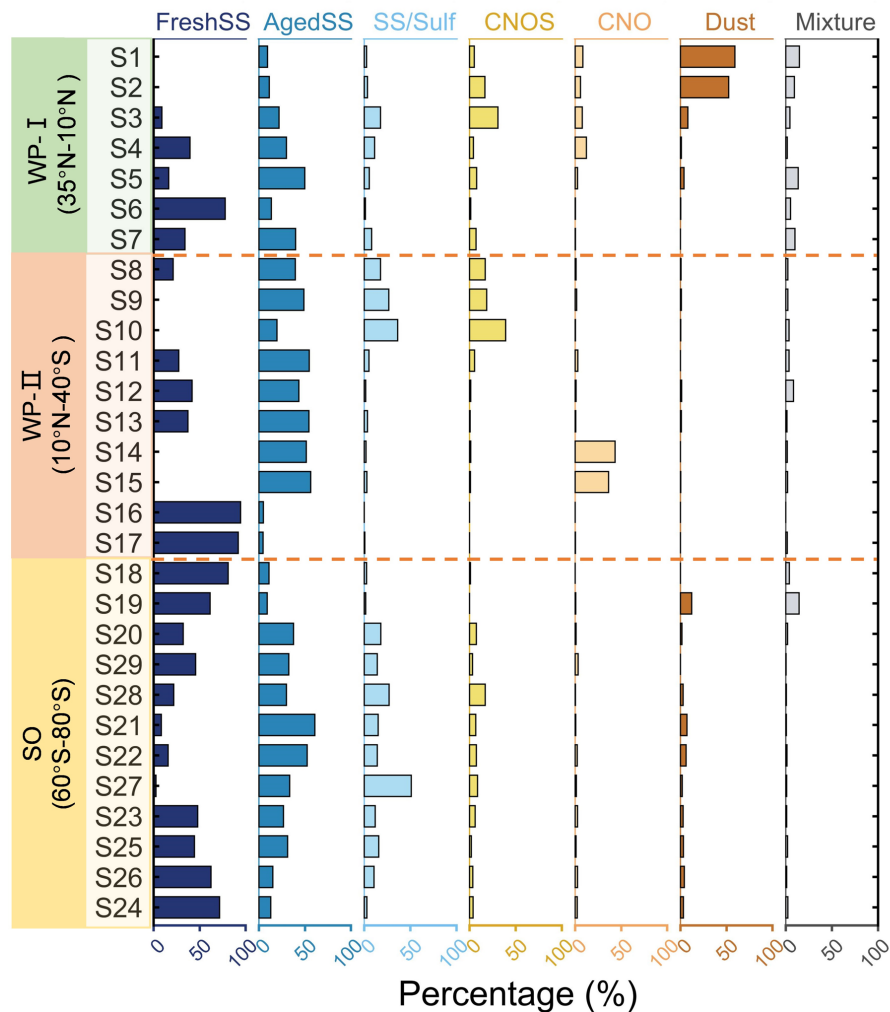
Figure 4. Relative percentages of the seven particle classes (FreshSS, AgedSS, SS/Sulf, CNOS, CNO, Dust, and Mixture) for each sample sorted by the latitudes of sampling locations and separated into three regions (see Fig. 1).

In the WP-II region (10°N – 40°S, S8 – S17), the backward trajectories (Fig. 1) display that the air mass of most samples resided over the ocean. However, the samples demonstrated large variations in the particle composition. S8 – S10 were dominated by AgedSS, SS/Sulf, and CNOS particles. The percentage of SS/Sulf and CNOS particles increased from 18% to 36% and from 17% to 39%, respectively, from S8 to S10. The contributions of these two sulfur-containing particle classes increased simultaneously, implying the same sulfur source. This is consistent with the results showing high sulfate aerosol optical depth (AOD) from the NAAPS-RA products at the same period (Fig. S4D – F). The average BC concentration was 107.4 ± 70.6 ng/m^3 for S8 (Table S1). It

likely originated from combustion emissions transported from land. As shown in Fig. S4C, this is further supported by the air mass for S8 passed through the region where fire spots were detected in NASA Fire Information for Resource Management System (FIRMS). S14 and S15 were dominated only by the AgedSS and CNO particles, with the latter accounting for 43% and 36%, respectively. These higher fractions of CNO particles compared to other samples (Fig. 4) are likely related to BBA. As shown in Fig. S1, the average BC concentrations of S14 and S15 were as high as 674 and 356 ng m^{-3}, respectively. Backward trajectories showed that the air mass passed through the high smoke AOD regions (Fig. S4G – H). These two samples were collected on November 13th and 14th of 2019, when large wildfires occurred in Australia during the austral summer of 2019 – 2020 (Hirsch and Koren, 2021). Dense fire spots along the east coast of Australia at the time of sampling are shown in Fig. S4I. Chemical imaging of elements (Fig. S5) showed that typical CNO particles from these two samples had thick organic coatings with high carbon signal inclusions and likely are aged BC. This type of aged BBA or smoke particles with organic coatings has been observed in the stratosphere (Ditas et al., 2018). Similar complex organic compounds have also been observed in the tropospheric smoke aerosol (Palm et al., 2020). Other samples in the WP-II region (S11, S12, S13, S16, and S17) were dominated by the FreshSS and AgedSS particles.

In the SO region (60°S – 80°S, sample S18 – S24), the number percentages of FreshSS particles decreased first and then increased as moving toward higher latitude, whereas the AgedSS, SS/Sulf, and CNOS particles had opposite trends. These three particle types contributed to 11% to 93% of the total particles in the sample. As shown in Fig. S6, the contributions of AgedSS, SS/Sulf, and CNOS particles from the middle of the Ross Sea (S28, S21, S22, S27, S23) were significantly higher than those from the north (S18, S19, S20, S29) and southwest (S25, S26, S24) of the Ross Sea. The increased contribution of these three sulfur-containing particle classes may be related to the biogenic sulfur emission from polynyas (areas of open water surrounded by sea ice) in the central Ross Sea (Fig. S7) (Brean et al., 2021; Baccarini et al., 2021; McCoy et al.,

449   2021; Jang et al., 2019; Zhang et al., 2015). The formation of polynyas during the

450   austral summer allowed phytoplankton to grow and produce DMS. DMS is transferred

451   into the atmosphere and oxidized. The products increase the sulfur content in aerosol

452   particles. Previous works indicated that the MSA concentration over the Southern

453   Ocean was about two times higher than that of the Western Pacific (Kunwar et al., 2023).

454   High MSA levels were observed in the Ross Sea and were associated with the dynamic

455   sea ice edge at ~64°S in early December (Yan et al., 2020). This was caused by the

456   increase in phytoplankton from the release of algae from the melting sea ice. This also

457   suggests the potential impacts by the biogenic emission of DMS on these samples.

458

459   Except for the two samples impacted by the dust storm, most of the samples collected

460   during this cruise were predominantly sea salt containing particles including the

461   FreshSS, AgedSS, and SS/Sulf classes, with total number percentages ranging from 48%

462   to 99%. The varying proportions of these three particle classes indicated the

463   contribution of marine emission, but with different degrees of aging which will be

464   discussed in the next section. Figure S8A and Fig. S9A show the classification results

465   for super-micron particles (diameter > 1 μm) and submicron particles (diameter

466   between 0.2 and 1 μm), respectively. The sea salt containing particles including

467   FreshSS, AgedSS, and SS/Sulf classes had higher percentages in the super-micron size

468   range. The majority of CNOS particles were in the submicron size range. CNOS

469   represents sulfur containing particles (e.g., sulfate) including their mixtures with

470   organics. CNOS particles were predominantly in the submicron range, likely due to

471   new particle formation of MSA and H_2SO_4 and their condensation onto pre-existing

472   particles (Hopkins et al., 2008; Yan et al., 2020; Beck et al., 2021). Heterogeneous

473   aqueous chemical reactions may also contribute to CNOS particles, including cloud

474   processing (e.g., Ervens et al., 2018).

475
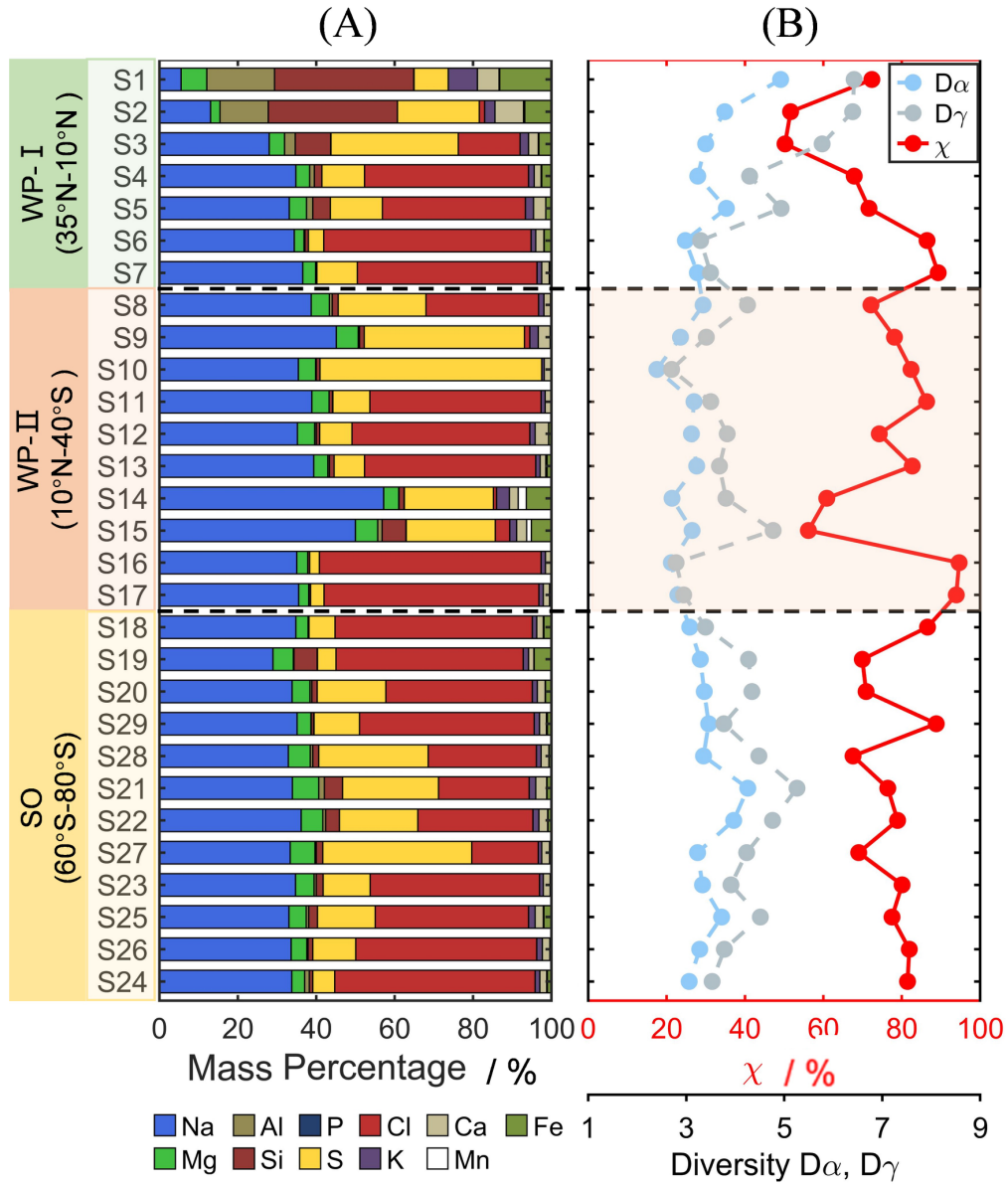
Figure 5. Relative mass percentages of elements (A), and mixing state (B) of all samples. Color codes for the elements are shown at bottom. Light blue, gray, and red circles represent the particle elemental diversity (D_α), population elemental diversity (D_γ), and mixing state index (χ), respectively.

3.2 Mixing state of particle population

Mixing state described here is based on the elemental composition and is referred to as the chemical mixing state. Figure 5A shows the elemental mass percentages of the particle population for each sample. Most of the samples were dominated by Na, Cl, and S, except the samples affected by dust storm (S1, S2). The proportion of Na in each

487 sample was relatively stable at about 38%. The rest was contributed mostly by Cl and

488 S. The aging of sea salt particles can be evaluated by the elemental ratio of Cl to Na

489 (Cl/Na). As shown in Fig. 5A and Fig. S10, the Cl/Na ratio ranges from 0 to close to 1

490 indicating complete Cl depletion and no aging on sea salt particles, respectively. The

491 samples with more S have less Cl. This is consistent with the increase in the proportion

492 of sea salt with different degrees of aging (AgedSS and SS/Sulf). The relationship

493 between S and Cl indicates that the chlorine loss in particles over ocean is attributed to

494 the acid displacement by H_2SO_4 and MSA. The samples affected by the dust storm were

495 dominated by the elements of Si, Al, and Fe, all of which were common in mineral dust

496 with traces of Ca and K. As the elements of C, N, and O were not considered in the

497 mass percentage calculation, the CNO particles prominent in S14 and S15 are not

498 reflected in the mass percentages (Fig. 5A). The elements of K, Si, and Fe presented in

499 the same samples are related to biomass burning (Chen et al., 2017). It is consistent

500 with the air mass from which they were sampled being impacted by biomass burning

501 plumes.

502

503 The mixing state parameters, namely D_α, D_γ, and χ for each sample, are presented in

504 Fig. 5B. The range of D_α and D_γ was from 2.4 to 4.9 and 2.7 to 6.4, respectively. χ

505 ranged from 50% to 95%. In the WP-I region, the Dust-dominated S1 had the highest

506 D_α of 4.9 and D_γ of 6.4. As the contribution of the Dust particles decreased from 59%

507 to 1% for S1 to S4, D_α and D_γ decreased from 4.9 to 3.2 and 6.4 to 4.3, respectively. χ

508 first decreased from 72% to 50% (S1 to S3) and then increased to 68% (S4) as the

509 dominant particle type switched from Dust to sea salt containing particles. χ further

510 increased to 86% (S6) when FreshSS particles dominated. In the WP-II region, D_α and

511 D_γ decreased as CNOS and SS/Sulf particles increased and the mass percentage of S

512 increased from S8 to S10, corresponding to a slight increase in χ from 72% to 82%.

513 When comparing the wildfire-influenced samples (S14, S15) and the FreshSS

514 dominated samples (S16, S17), the D_α values are very similar whereas D_γ values are

515 quite different (3.8 and 4.8 vs. 2.8 and 2.9) resulting in contrasting χ values. The highest

516 χ of about 95% for S16 and S17 indicated that these two samples dominated by Na and

Cl were largely internally mixed. This can be expected since they were dominated by FreshSS particles from the single marine source. AgedSS particles from marine emission with additional atmospheric processing and CNO particles from biomass burning had similar contributions to S14 and S15. This was reflected in χ of about 58% for S14 and S15. The main elements of Na and S in these two samples are more externally mixed. In the SO region, D_α and D_γ were similar to each other resulting in relatively stable χ values. The changes in D_α and D_γ are mainly due to the changes in the contribution of sulfur containing particles. Figure S8 and Fig. S9 show the elemental mass percentages, D_α, D_γ, and χ for super-micron and submicron particles, respectively. For submicron particles of each sample, D_α and D_γ are 1.9 – 3.9 and 2.4 – 7.1, respectively. χ ranges from about 38% to 95%. For super-micron particles of each sample, D_α and D_γ are 2.5 – 5.1 and 2.7 – 6.6, respectively. χ ranges from about 54% – 96%. In general, D_α and χ for the submicron particles are lower than super-micron particles in most samples, whereas D_γ is similar. This suggests that the main elements of Na, S, and Cl and the minor elements of Mg, K, Fe, Ca, and Si in super-micron particles tend to be more internally mixed than in submicron particles (Fig. S8B and Fig. S9B).

The changes in the particle composition may affect the mixing state of the particle population. To focus on the effect of particle aging on the mixing state of marine aerosols, we excluded four samples from two events from the analysis, i.e., the Dust-dominated samples from a dust storm (S1 and S2) and the BBA-dominated samples from wildfire emissions (S14 and S15). Figure 6 shows the relationship between χ and the percentages of FreshSS, AgedSS and SS/Sulf, and CNOS particles in different size ranges. To minimize the potential influence of extreme data points, the linear regression was performed using the binned data based on the number percentage of particle type. We found a strong correlation between the percentages of FreshSS particles in the samples and their χ (Fig. 6A, $R^2 = 0.66$, $p = 0.008$), especially for submicron particles ($R^2 = 0.85$). χ increased as the contribution of FreshSS particles increased. There is a negative correlation between χ and the total percentage of AgedSS and SS/Sulf particles

547 (Fig. 6B, $R^2 = 0.46$, $p < 0.05$). We also found a strong negative correlation between χ

548 and the contribution of CNOS particles (Fig.6C, $R^2 = 0.86$, $p = 0.002$). The results of

549 the above-mentioned relationship also hold for both submicron and super-micron size

550 range particles. The positive correlation between the contribution of FreshSS particles

551 and χ indicates that the particle population became more internally mixed as more fresh

552 SSA were added to the air parcel. When the FreshSS particles became the dominant

553 type, the particle population was close to the complete internal mixing ($\chi = 100\%$), such

554 as S16 and S17 as discussed above. Here, we show that adding more particles of the

555 dominant particle class (FreshSS) makes the population more internally mixed. Adding

556 CNOS particles (a new particle class) decreases the χ and makes the population more

557 externally mixed. These results verify the schematic description of the evolution of the

558 mixing state described by Riemer et al. (2019). It states that adding new particle types

559 makes the population more externally mixed and adding particles of a dominant particle

560 type makes the population more internally mixed.

561

562
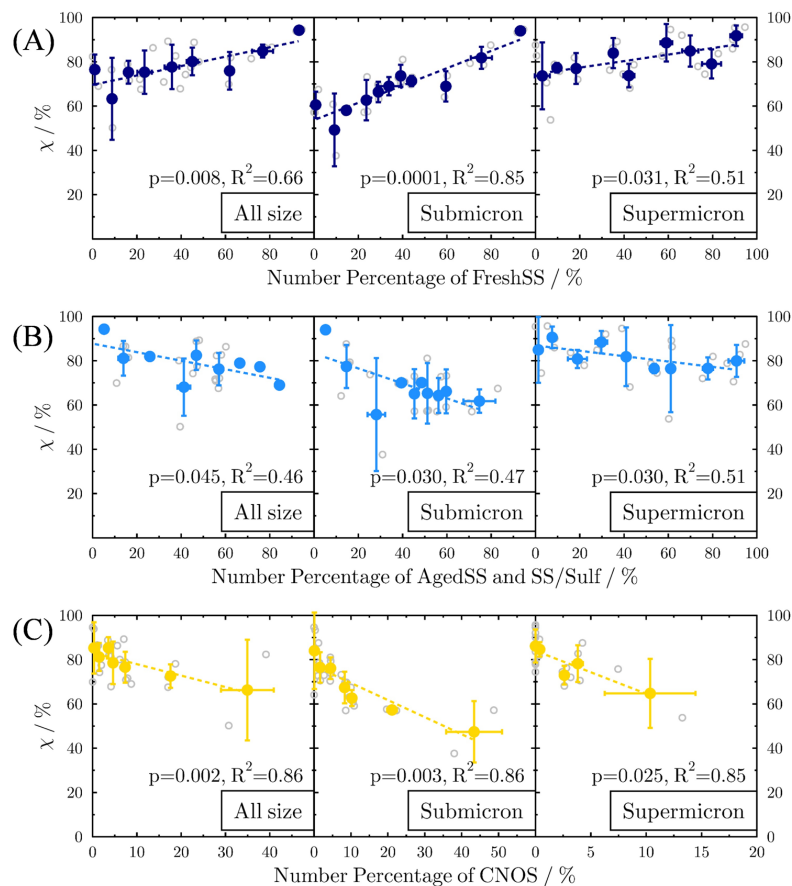
Figure 6. Variation of mixing state index (χ) with the number percentages of different particle classes: (A) FreshSS, (B) AgedSS and SS/Sulf, and (C) CNOS. Panels from left to right are for particles with different size ranges: all particle size (All size), $0.2 - 1$ μm (Submicron), and larger than 1 μm in diameter (Super-micron). Original and binned data are shown in open circles and solid color circles, respectively. Linear regression (dash line) is based on the binned data.

Atmospheric aging processes can change the composition and mixing state of aerosol population. In marine environments, the degree of aging on sea salt particles can be reflected by the contribution of AgedSS and SS/Sulf particles in the population. The negative correlation between the number percentages of AgedSS and SS/Sulf particles and χ indicates that aging has resulted in a more externally mixed particle population. This seems to contradict the view that aging tends to drive a particle population towards a more internally mixed state (Riemer et al., 2019). If an aging process (e.g., condensation of secondary organics) occurs uniformly on each particle and further aging makes them more homogeneous, the population tends to be more internally mixed. On the other hand, if the aging process occurs only on a specific type of particle, such as acid displacement turning fresh sea salt into aged sea salt, this will increase particle diversity and the population may move to a more externally mixed state. This may be particularly true as fresh sea salt is continuously released even as aged sea salt particles form. The availability of acids and the size distribution of fresh and aged sea salt particles at different locations could result in particles with different chlorine deficiencies and greater diversity. In this case, aging will increase the inhomogeneity of particles and move the population toward a more externally mixed state.

3.3 Ice nucleation properties at cirrus conditions

We conducted ice nucleation experiments on six samples dominated by different particle classes. These samples are separated into four groups: *i*) Dust dominated sample (S1), where 59% of the particles are dust-like. *ii*) BBA influenced sample (S14). This sample was affected by biomass burning. CNO and AgedSS particles contributed 43% and 51%, respectively. *iii*) CNOS and SS/Sulf dominated sample (S10) with

percentages of 39% and 36%, respectively. *iv*) FreshSS and AgedSS dominated samples (S4, S11, and S12). The number percentages of the FreshSS and AgedSS particles are 70%, 82%, and 85% for S4, S11, and S12, respectively. Table 1 shows the dominant particle class, total particle surface area, number of particles available for ice nucleation during the experiments, IN-activated fraction at ice nucleation onsets, average ECD of INPs and non-INPs, and average ECD of INPs.

Table 1. Information of particle samples including the total particle surface area and number of particles, IN-activated fraction at ice nucleation onset conditions, the average ECD of INPs and non-INPs, and the average ECD of INPs.

Sample	Dominant particle type	Particle surface area ($\times 10^4$ μm^2)	Particle number ($\times 10^5$)	IN-activated fraction (‰)	ECD for INPs (μm)	ECD for all (μm)
WP-I-S1	Dust	4.35	0.85	0.12 − 0.24	2.53 ± 1.76	1.45 ± 0.98
WP-I-S4	FreshSS+AgedSS	0.54	1.29	0.08 − 0.15	0.99 ± 0.25	0.89 ± 0.25
WP-II-S10	CNOS+SS/Sulf	6.81	9.13	0.01 − 0.03	1.54 ± 0.56	1.21 ± 0.57
WP-II-S11	FreshSS+AgedSS	7.76	6.37	0.02 − 0.03	1.19 ± 0.63	1.03 ± 0.50
WP-II-S12	FreshSS+AgedSS	12.91	8.26	0.01 − 0.02	1.91 ± 1.20	1.22 ± 0.78
WP-II-S14	BBA	13.84	0.56	0.18	5.17 ± 3.12	2.50 ± 2.01

Figure 7 shows the onset conditions of T_p and RH_{ice} for water uptake and ice nucleation on the representative samples. Below 235 K, only DIN was observed for the Dust and BBA samples (Fig. 7A). Particles on the Dust sample nucleated ice heterogeneously at RH_{ice} from 130% ± 9% to 153% ± 8% at T_p from 235 K to 209 K. These values are below the homogeneous nucleation limits of aqueous droplets (Koop et al., 2000; Koop and Zobrist, 2009). RH_{ice} onsets of the BBA sample ranged from 145% ± 5% to 169% ± 1% at T_p from 229 K to 209 K. The RH_{ice} onsets were only about 3% below the homogeneous nucleation limits between 220 K and 228 K, and thus the sample dominated by BBA may not have been efficient heterogeneous ice nuclei. As T_p decreased, the RH_{ice} onset of both the BBA and Dust samples gradually increased. Particles on the Dust sample initiated DIN at RH_{ice} lower than the BBA sample by 7% to18% at each T_p. For the CNOS and SS/Sulf dominated sample (Fig. 7A), particles first took up water when RH_w reached about 83% and then froze via IMF or

homogeneous nucleation with RH_{ice} around the homogeneous line at the temperature close to 230 K. Particles formed ice via DIN below 225 K at RH_{ice} from 136% ± 4% to 159% ± 11%. Figure 7B shows that the ice nucleated on particles from the FreshSS and AgedSS dominated samples via DIN and IMF pathways. The transition temperature between DIN and IMF pathways was about 225 K. At about 225 K, particles on S4 and S12 both took up water at 78% ± 2% and then formed ice upon further cooling. The subsequent ice nucleation of S12 could be homogeneous nucleation or IMF since the onset RH_{ice} of 150% ± 7% is close to the homogeneous nucleation limit. However, particles of S4 nucleated ice after water uptake through IMF at RH_{ice} of 140% ± 8% which is about 8% lower than the homogeneous nucleation limit. Below 225 K, particles of S4 and S12 nucleated ice via DIN at RH_{ice} from 133% ± 4% to 170% ± 8%. DIN occurred on the S11 particles at about 121% ± 3% to 130% ± 3% RH_{ice} below 225 K. S11 showed the lowest onset RH_{ice} among the investigated samples indicating that its ice nucleation efficiency was higher than other samples. The results of ice nucleation onset conditions for the investigated samples showed distinct variations in the ice nucleation ability for particles in the different marine atmospheres, even for the samples (S11, S12) with similar elemental composition and the dominant particle classes. The possible reasons for this are discussed in the later section.
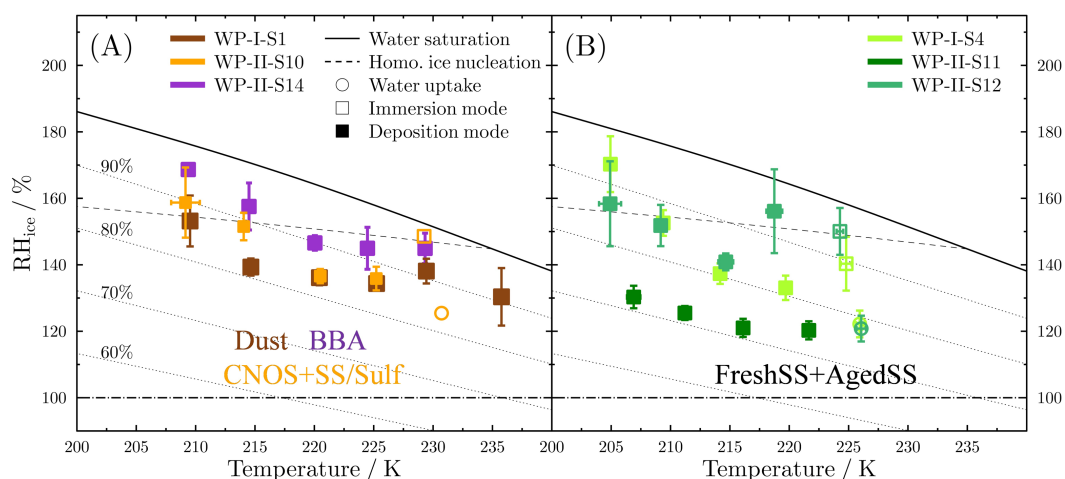
Figure 7. Onset conditions of freezing temperature and RH_{ice} for water uptake (open circles), immersion freezing (open squares), and deposition ice nucleation (solid squares) on particle samples. (**A**) Dust dominated sample (S1), BBA influenced sample (S14), and CNOS and SS/Sulf dominated

639   sample (S10); (B) FreshSS and AgedSS dominated samples (S4, S11, S12). Dashed line indicates

640   the homogeneous freezing limits for aqueous droplets of 0.3 μm in diameter (Koop et al., 2000;

641   Koop and Zobrist, 2009). Dotted lines represent different relative humidity (RH_w) shown in panel

642   A. Solid and dased-dotted lines represent water saturation (100% RH_w) and ice saturation (100%

643   RH_{ice}), respectively.

644

645   **3.4 INP characterization**

646   In total, 132 INPs together with 1317 non-INPs on the silicon wafer substrates were

647   identified and characterized individually for their morphology and elemental

648   composition. Figure 8 shows the representative SEM images and the corresponding

649   EDX spectra of different types of INPs. SEM images for each identified INP at different

650   temperatures are shown in Figs. S11, S12, and S13. The average ECD of INPs was

651   generally greater than the ECD of the population considering both INPs and non-INPs

652   together for each sample (Table 1). Of the 132 INPs, 71% of them were super-micron

653   particles and the rest were submicron particles. The INPs exhibited different

654   morphologies, such as crystalline irregular shapes (e.g., INPs classified as FreshSS,

655   Aged SS, and Dust) and spherical shapes (e.g., INPs classified as CNOS). We found

656   that the majority of INPs from S14 influenced by BBA had thick organic coatings (Fig.

657   8 and Fig. S11). The organic coating thickness of BBA INPs (1.07 ± 0.68 μm, n = 13)

658   is significantly thicker than that of other BBA (0.53 ± 0.37 μm, n = 112) at the

659   significant level of 0.001. Different number fractions of INPs identified in the FreshSS

660   and AgedSS dominated samples (S4, S11, and S12) have organic coatings. More than

661   80% of INPs in S11 were coated with organics compared to S4 (33%) and S12 (30%).

662   Figure S14 shows the elemental mapping of a representative INP with a thin organic

663   coating. The mapping shows that Na and Cl were distributed in the core, while C and

664   O were present throughout the whole 2-D projected area of this AgedSS INP. Previous

665   studies have shown that solid organics can form ice via DIN at low temperatures (Wang

666   et al., 2012b; Knopf et al., 2018; Lata et al., 2021; Alpert et al., 2022). We speculate

667   that the organic coatings on the particles of S11 triggered the ice nucleation which have

668   different ice nucleation abilities compared to S4 and S12.
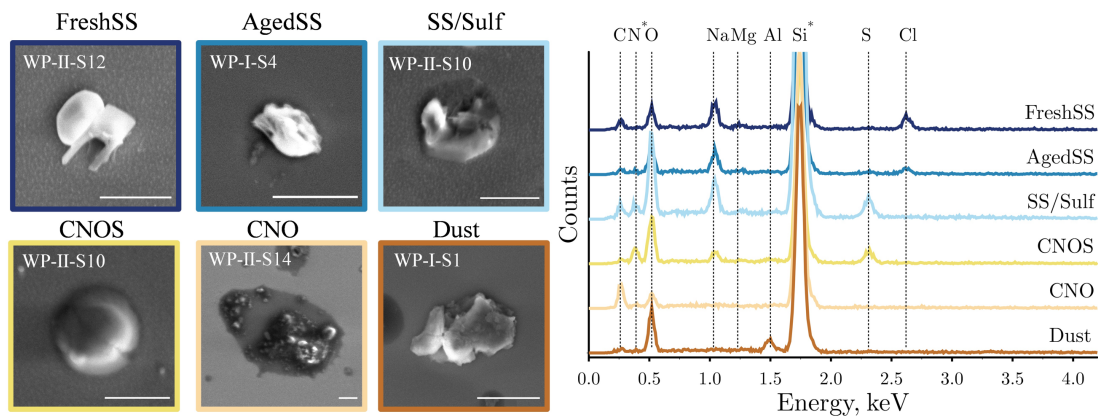
Figure 8. Representative SEM images and the corresponding EDX spectra for 6 classes of INPs. The spectra include the substrate background signal of N and Si (asterisked) from silicon wafer coated with Si_3N_4. Labels on SEM images are the name of samples. Scale bar is 2 μm for all images.

All the identified INPs and non-INPs on the substrates used in the ice nucleation experiments were categorized based on the SEM/EDX data. Figure 9 shows the percentages of different classes for INPs and the particle population in stacked bars marked with "INPs" and "All", respectively. Taking S1 as an example, six particle classes were identified in the particle population and the 19 identified INPs are from five particle classes except for the CNO class. Similar to S1, the dominant particle classes in the population of all respective samples are also the dominant classes of INPs. This result suggests that all these major particle classes identified in our experiments are potential INPs. We calculated the average elemental composition of INPs and non-INPs for each particle type as shown in Fig. S15. A two-sample t-test was also performed on the elemental compositions of INPs and non-INPs for each particle type. At the significant level of 0.05, there is no sufficient evidence showing that the elemental compositions of INPs and non-INPs are different. We also found that the contributions of the same particle class in INPs and the particle population are different in some cases. The most notable example is S10 where SS/Sulf particles contributed 77% of INPs, but only 51% of the population.
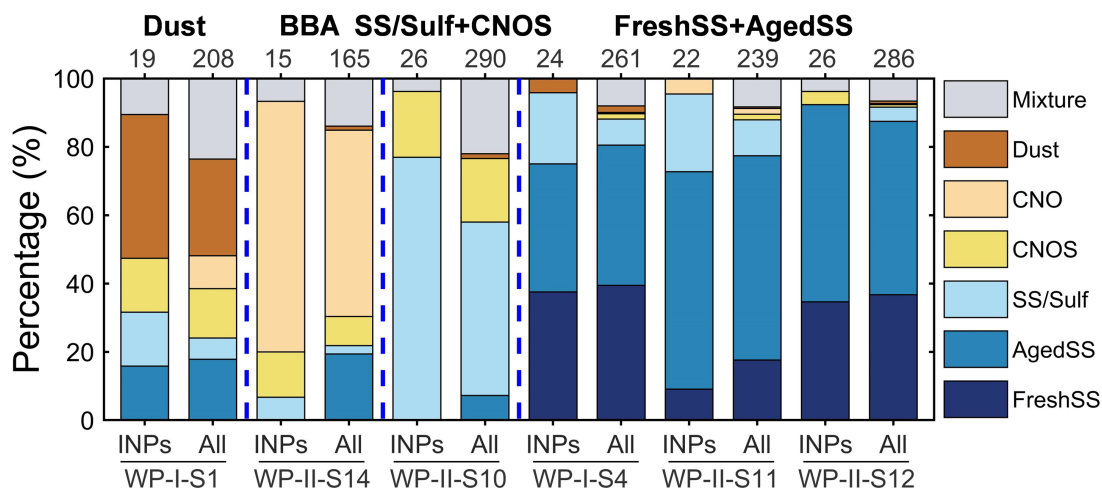
Figure 9. The number percentages of different particle classes for INPs and the particle population. Data marked with "All" including both INPs and non-INPs. The corresponding numbers on the top represent the investigated particle number. Blue dashed lines separate the samples with different particle classes.

To further explore whether a particle class is unique when acting as INPs, we calculated the enrichment factor (*EF*) for a given particle class (A) according to the following formula:

$$EF(\text{A}) = \frac{\left(\dfrac{N_{\text{INPs}}^{\text{A}}}{N_{\text{INPs}}}\right)}{\left(\dfrac{N_{\text{INPs+non-INPs}}^{\text{A}}}{N_{\text{INPs+non-INPs}}}\right)} \tag{14}$$

where N is the number of particles. *EF*(A) is the ratio of the contributions of the particle class A in the INPs to the whole particle population (INPs + non-INPs). *EF* values of each particle class for different samples are shown in Fig. 10. *EF* values with upper and lower limits determined from Poisson distributed errors at 95% confidence level are listed in Table S2. Although the enriched particle classes are diverse for different samples, *EF* of the SS/Sulf class is greater than 1 for most of the samples except S12. No INP was identified as SS/Sulf particle for S12 which only has 4% of SS/Sulf in the population. The overall *EF* of the SS/Sulf class is 1.9 with the upper and lower limits of 9.2 and 1.2, respectively. This indicates that the SS/Sulf particles were enriched in INPs in these marine environments.

710
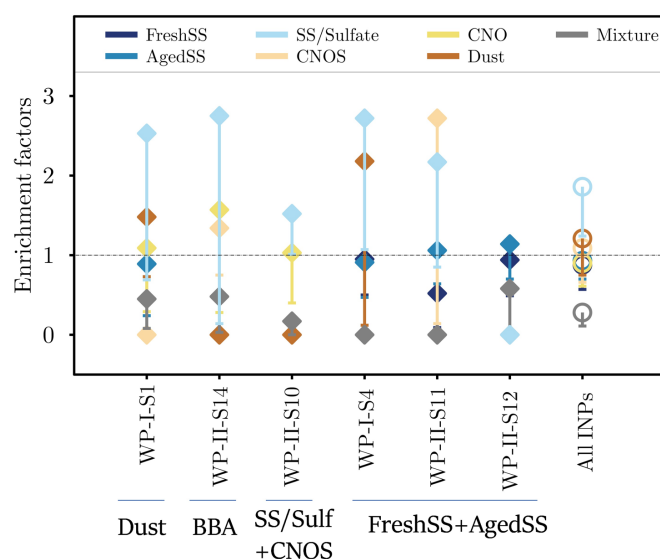
Figure 10. The *EF* of all INP classes for each sample (solid diamonds) and all INPs (open circles).

The dashed line indicates *EF* of 1. The lower limits of *EF* were calculated by Poisson distribution

at the confidence level of 95%. For the readability, the upper limits were not plotted here but the

values are listed in Table S2.

715

3.5 Comparison of ice nucleation properties with previous studies

Figure 11 shows the comparison of ice nucleation data from our work and previous

studies. The DIN onset conditions of the Dust dominated sample (S1) are similar to the

feldspar between 230 K and 235 K (Yakobi-Hancock et al., 2013) and less efficient

compared to bare dust particles, including montmorillonite (Welti et al., 2009; Kulkarni

et al., 2014), illite (Welti et al., 2009; Kulkarni et al., 2014), quartz (Kulkarni et al.,

2014), and kaolinite (Wang and Knopf, 2011). Previous laboratory studies showed that

the aging processes can reduce the ice nucleation ability of mineral dust at temperatures

relevant to cirrus clouds (Tang et al., 2016). For example, Primm et al. (2017) indicated

that the ice nucleation ability of illite can be slightly suppressed by organic acids when

mixed with a mixture of five dicarboxylic acids (referred to as M5) at an organic-illite

mass ratio greater than 1:1. The DIN onset conditions of S1 are similar to the M5/illite

(10:1) mixtures (Fig. 11A). We also found that coated particles (Fig. S16) in S1 serving

as INPs have a similar coating thickness (Fig. S11) as organic coatings on M5/illite

greater than 1:1. Kulkarni et al. (2014) observed a decrease in ice nucleation ability of montmorillonite, illite, and quartz at 235 K when coated with H_2SO_4. These H_2SO_4 coated dust particles had a similar onset RH_{ice} as compared to particles on S1 at 235 K. During the cruise, S1 and S2 in the WP-I region were impacted by the dust storm originating from western Asia. The dust particles were aged during the transport to the coastal areas and some of them had clear coatings (Fig. S11 and Fig. S16). This is consistent with the finding by Jang et al.(2023) from the same cruise that aerosol particles in the S1 sample area have a high fraction of lignin-like organics. S1 had a similar ice nucleation ability as dust particles with organic coatings. We suspect that the ice nucleation efficiency of the dust particles at temperatures where DIN occurred on the INP's surface was affected by coatings after aging.

Our results for S14 suggest that BBA from the Australian wildfires may have served as INPs via DIN below 230 K. Combustion and burning processes produce a large number of particles with mixed organic and inorganic components into the atmosphere (e.g., Fuzzi et al., 2007; Chen et al., 2017; Hodshire et al., 2019). Previous studies have shown that soot, combustion ash, and BBA particles from different burning sources demonstrated various ice nucleation properties (e.g., Jahl et al., 2021; Jahn et al., 2020; Kanji et al., 2017 and references therein). Soot particles or their organic coatings on S14 may have played a role in the observed ice nucleation events. Several studies have reported that combustion related particles can serve as INPs via DIN below 233 K (DeMott et al., 1999; Möhler et al., 2005a, b; Koehler et al., 2009; Kanji et al., 2011; Chou et al., 2013). Kanji et al. (2011) showed the ice nucleation activated by soot generated using a graphite spark generator (GSG) at about 145% RH_{ice}, a value similar to S14 at 230 K. Chou et al. (2013) showed that wood burning particles nucleated ice at about 136% RH_{ice} at about 233 K. DeMott et al. (1999) reported that the freezing RH_{ice} of soot was close to the homogeneous freezing limits. S14 nucleated ice at higher RH_{ice} than soot generated by GSG and particles containing organic carbon (Möhler et al., 2005a, b), but lower than the soot studied by DeMott et al. (1999). Suwannee River standard fulvic acid (SRFA) and leonardite were used as surrogates of atmospheric

organize from biomass burning (Wang and Knopf, 2011). Ice nucleation onset
conditions of S14 are very similar to those of SRFA and ozone aged leonardite particles
above 220 K but higher at lower temperatures.
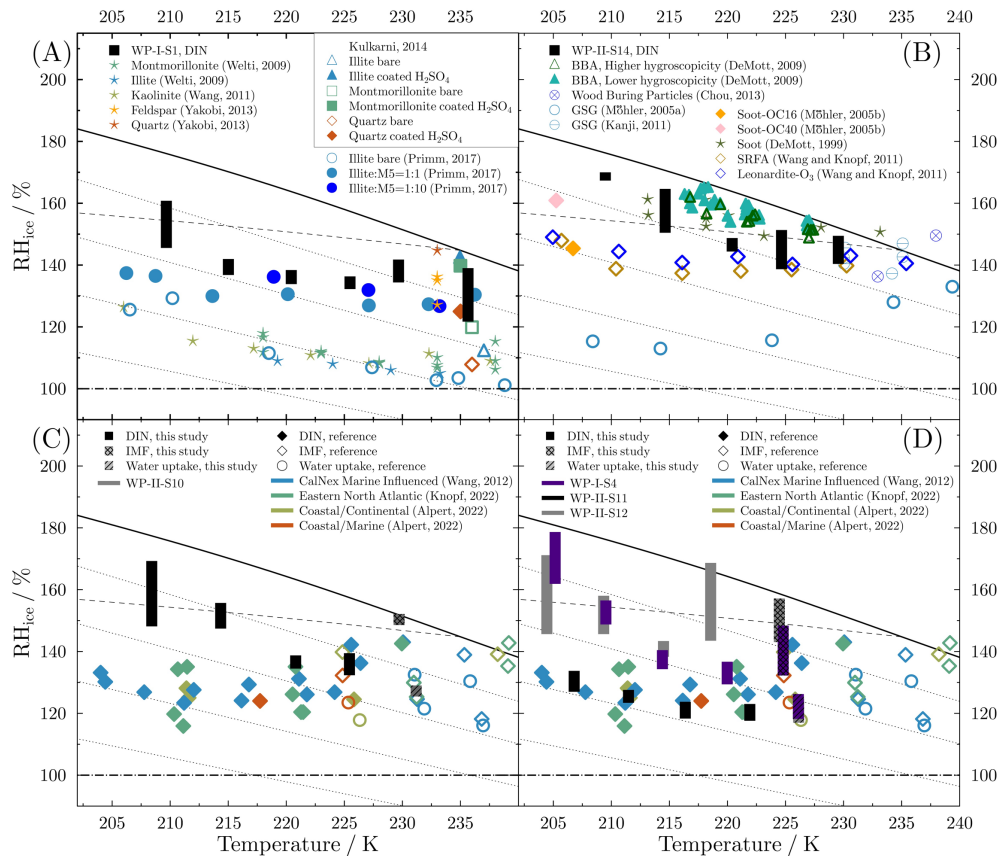
Figure 11. Ice nucleation and water uptake onset conditions (bars) for (A) Dust dominated sample
(S1), (B) BBA influenced sample (S14), (C) CNOS and SS/Sulf dominated sample (S10), and (D)
FreshSS and AgedSS dominated samples (S4, S11, S12) compared with previous studies (symbols)
(DeMott et al., 1999, 2009; Möhler et al., 2005a, b; Welti et al., 2009; Kanji et al., 2011; Wang and
Knopf, 2011; Wang et al., 2012a; Yakobi-Hancock et al., 2013; Kulkarni et al., 2014; Primm et al.,
2017; Alpert et al., 2022; Knopf et al., 2022). Descriptions for the lines are the same as in Fig. 7.

Figures 11C and 11D show the comparison of data on marine related particles from
previous studies with our data on sea salt containing particles. Several studies have
shown that the aerosol particles collected in marine environments or coastal areas can
act as efficient INPs at RH_{ice} between 115% and 143% (e.g., Wang et al., 2012a; Alpert
et al., 2022; Knopf et al., 2022). Using the micro-spectroscopic analysis, these studies

776   identified the INPs and demonstrated that the major particle types in the population

777   initiate ice formation. These particle types include the marine influenced particles with

778   thin organic coatings collected during the CalNex field campaign (Wang et al., 2012a),

779   the relatively fresh sea salt particles with marine-produced organics collected from the

780   coast of Long Island, New York (Alpert et al., 2022), and the processed sea salt

781   containing particles collected over the eastern North Atlantic (Knopf et al., 2022). There

782   is one FreshSS and AgedSS dominated sample (S11) that nucleated ice at the same

783   RH_{ice} onsets as compared to those marine-influenced particles from above mentioned

784   studies. The other sea salt containing samples in this work including the CNOS and

785   SS/Sulf dominated sample (S10) and the FreshSS and AgedSS dominated samples (S4,

786   S12) showed very similar RH_{ice} onsets only at temperatures above 220 K but higher

787   onsets below 220 K. The reason for this discrepancy at lower temperatures is not clear.

788   Future work on the coating composition may provide more insight. Together with

789   previous studies, we show that these marine influenced particles exhibit different ice

790   nucleation efficiencies. These variations are likely contributed not only to the complex

791   compositions but also to the physical and chemical mixing state of these particles.

792

3.6 Ice nucleation kinetics

794   Ice nucleation kinetic analysis was conducted using the experimental data, including

795   the RH_{ice} and temperature onsets, particle surface area, number of nucleation events,

796   and nucleation time. Classical nucleation theory (CNT) has been widely used in cloud

797   models (e.g., Pruppacher and Klett, 2010; Khvorostyanov and Curry, 2004; Liu and

798   Penner, 2005). In this study, heterogeneous ice nucleation rate coefficient (J_{het}), contact

799   angle (θ), and their parameterizations are presented and discussed. Ice nucleation

800   activated fraction of each sample was listed in Table 1 and discussed in Text S2. n_s

801   based on the singular hypothesis (Vali, 1971; Connolly et al., 2009) and its

802   parameterizations are also presented in Text S2.

803

3.6.1 Heterogeneous ice nucleation rate coefficient (J_{het})

805 According to CNT, ice nucleation is a stochastic process and continues with time, in

806 contrast to the singular hypothesis (Pruppacher and Klett, 2010). J_{het} depends on

807 temperature and RH_{ice}. J_{het} was derived following the approach in previous works

808 (Wang and Knopf, 2011; Wang et al., 2012a; China et al., 2017; Knopf et al., 2022).

809 Using the observed ice nucleation data, $J_{het} = N_{ice}/(t \times A_{tot})$, where N_{ice} is the

810 number of the observed ice nucleation events that occurred in a temperature interval,

811 A_{tot} is the total particle surface area available for ice nucleation experiment in the

812 temperature interval, t of 6 seconds is the time interval between two consecutive OM

813 images used to monitor ice formation. In the four groups of particle samples we

814 investigated, J_{het} for DIN ranged from 130 to 1370 $cm^{-2} s^{-1}$, 40 to 2970 $cm^{-2} s^{-1}$, 40 to

815 1480 $cm^{-2} s^{-1}$, and 10 to 390 $cm^{-2} s^{-1}$ for the Dust dominated, BBA influenced, CNOS

816 and SS/Sulf dominated, and FreshSS and AgedSS dominated samples, respectively.

817 J_{het} for IMF ranged from 540 to 4780 $cm^{-2} s^{-1}$ for the FreshSS and AgedSS dominated

818 samples.

819

820 **3.6.2 Parameterizations of J_{het} and θ**

821 The experimentally derived J_{het} was parameterized based on the water-activity-based

822 approach. The water-activity-based approach has been widely used to describe the

823 homogeneous ice nucleation of droplets and depends only on a droplet's water activity

824 (a_w) and T_p (Koop et al., 2000). Homogeneous ice nucleation temperature follows a

825 single curve as a function of a_w and is parameterized by a constant shift of a_w (i.e.,

826 Δa_w) from the ice melting temperature curve (Koop and Zobrist, 2009). This approach

827 has also been applied to heterogeneous ice nucleation including DIN and IMF (Koop

828 and Zobrist, 2009; Knopf and Alpert, 2013; China et al., 2017). It is assumed that

829 particles were in equilibrium with the gas phase during the experiments, so $a_w =$

830 $RH_w/100$. For each nucleation event, $\Delta a_w(T_f)$ is the difference between the RH_w at

831 which ice nucleated and the RH_w on the ice melting curve at the observed ice nucleation

832 temperature (T_f), or $a_w(T_f)$ and $a_w^{ice}(T_f)$, respectively. Then, $\Delta a_w(T_f) = a_w^{ice}(T_f) -$

833 $a_w(T_f)$ (Knopf and Alpert, 2013; Koop and Zobrist, 2009), which can be calculated for

834 each ice nucleation event using the ice nucleation onset temperature and RH_w. J_{het} was

835   calculated for all ice nucleation events and parameterized as a function of Δa_{w}

836   following the previous works (China et al., 2017; Alpert et al., 2022; Knopf et al., 2022,

837   2023). Figure 12 presents the J_{het} (Δa_{w}) for the DIN and IMF data along with the

838   parameterizations according to $\log(J_{\mathrm{het}}) = c \times \Delta a_{\mathrm{w}} + d$. The values of c and d

839   parameters are listed in Table 2. The Dust dominated sample has higher J_{het} at the same

840   Δa_{w} compared with the other samples. The BBA influenced sample only nucleated ice

841   at higher Δa_{w}. The DIN J_{het} for the FreshSS and AgedSS samples changes by 2 orders

842   of magnitude over a wide range of Δa_{w}. For the FreshSS and AgedSS samples, IMF J_{het}

843   with a larger c displays a steeper slope than DIN J_{het}.

844

845   In Fig. 12, we compared our J_{het} parameterizations with previous studies. DIN J_{het} of

846   the Dust-dominated sample is similar to the particles collected during the Aerosol and

847   Cloud Experiments in the Eastern North Atlantic (ACE ENA) field campaign within

848   the marine boundary layer (ACE ENA MBL) (Knopf et al., 2022, 2023). It is about 1-

849   2 orders of magnitude lower than particles collected from the free troposphere (ACE

850   ENA FT). DIN J_{het} of the other particle types investigated in this study are lower than

851   particles collected from ACE ENA FT, ground site (ACE ENA GD), and ACE ENA

852   MBL. This is consistent with the results showing that our particles nucleated ice at

853   higher RH_{ice} than particles collected during ACE ENA (Fig. 11). DIN J_{het} for the

854   FreshSS and AgedSS samples is similar to the SSA investigated by Alpert et al. (2022)

855   in the lower Δa_{w} range (less than 0.25). This is likely because S11 nucleated ice in this

856   Δa_{w} range (i.e., RH_{ice}) is similar to the SSA INP investigated by Alpert et al. (2022) as

857   they have similar morphology and composition. IMF J_{het} of the FreshSS and AgedSS

858   samples is slightly higher than particles from ACE ENA GD and 1-2 orders of

859   magnitude higher than the other field samples (Fig. 12C). The IMF J_{het} of the FreshSS

860   and AgedSS samples displays a smaller slope with Δa_{w} compared to the laboratory-

861   generated particles, such as illite (Knopf and Alpert, 2013), natural dust (Alpert and

862   Knopf, 2016; Niemand et al., 2012), leonardite particles (Knopf and Alpert, 2013), and

863   diatomaceous material (Knopf and Alpert, 2013; Knopf et al., 2011; Alpert et al., 2011a,

864   b). This is consistent with the study by Knopf et al. (2022) which suggested that the

865   diversity of ambient particles exhibit different ice nucleation efficiencies compared to

866   single-component INP types studied in the laboratory at different temperature ranges.

867   Our results emphasize the importance of studying the ice nucleation ability of particles

868   and their parameterizations from different geological areas with different diversities in

869   particle characteristics.
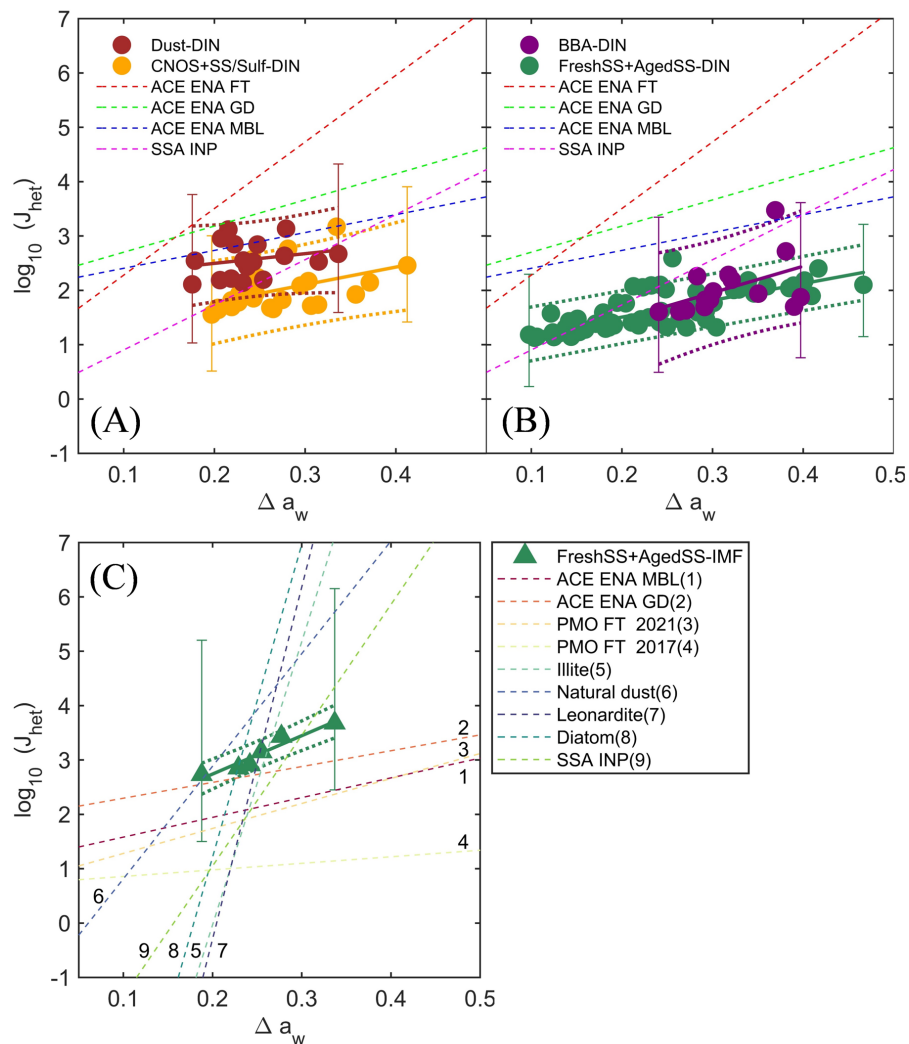
870

871 **Figure 12.** J_{het} as a function of Δa_w. Circles represent DIN J_{het} for (A) Dust, CNOS and SS/Sulf

872   dominated samples, (B) BBA, FreshSS and AgedSS dominated samples. Triangles represent IMF

873   J_{het} (C) for FreshSS and AgedSS dominated samples. Solid lines indicate the fittings according to

874      $\log(J_{het}) = c \times \Delta a_w + d$ with associated dotted lines representing the 95% prediction intervals.

875   Representative ΔJ_{het} (error bars) are plotted (Text S2). (A-B) Dashed red, green, and blue lines

876   represent DIN J_{het} parameterizations of particles collected from ACE ENA FT (Knopf et al., 2023),

877   ACE ENA GD (Knopf et al., 2022), and ACE ENA MBL (Knopf et al., 2023), respectively. Dashed

878   magenta line indicates J_{het} for SSA INPs (Alpert et al., 2022). (C) Dashed lines with the number

879   label of 1-4 represent IMF J_{het} for particles from ACE ENA MBL (Knopf et al., 2023), ACE-ENA

880   GD (Knopf et al., 2022), and the Pico Mountain Observatory (PMO) under free-troposheric (FT)

881   conditions in the Azores (PMO FT 2017 and PMO FT 2021) (China et al., 2017; Lata et al., 2021),

882   respectively. Dashed lines with the number label of 5-8 represent IMF J_{het} for illite particles (Knopf

883   and Alpert, 2013), natural dust (Alpert and Knopf, 2016; Niemand et al., 2012), leonardite particles

884   (Knopf and Alpert, 2013), diatomaceous material (Diatom) (Knopf and Alpert, 2013; Knopf et al.,

885   2011; Alpert et al., 2011a, b), and SSA INP (Alpert et al., 2022), respectively.

886

887   **Table 2** The c and d values for the parameterizations of J_{het} as a function of Δa_w,

888     $$\log(J_{het}) = c \times \Delta a_w + d.$$

Sample type	c	LCL$_c$	UCL$_c$	d	LCL$_d$	UCL$_d$	RMSE
Dust-DIN	1.78	− 0.15	3.72	2.14	1.67	2.61	0.31
BBA-DIN	4.88	2.38	7.39	0.49	− 0.31	1.30	0.43
CNOS+SS/Sulf-DIN	3.24	1.91	4.57	1.13	0.77	1.50	0.35
FreshSS+AgedSS-DIN	3.09	2.76	3.42	0.89	0.81	0.97	0.24
FreshSS+AgedSS-IMF	7.06	6.03	8.09	1.33	1.06	1.60	0.09

889

890   θ for DIN is derived based on CNT following our previous studies (Wang and Knopf,

891   2011; Wang et al., 2012a). θ is calculated from J_{het} and the ice nucleation onset

892   temperature and RH_{ice} using the following formula: $J_{het} = A \times \exp\left(\frac{-\Delta F_{g,het}}{kT}\right)$, where

893   A is a pre-exponential factor and k is the Boltzmann constant. $\Delta F_{g,het}$ is the free energy

894   of ice embryo formation, which is defined as $\Delta F_{g,het} = \frac{16\pi M_w^2 \sigma_{i/v}^3}{3[RT\rho \ln S_{ice}]^2} \times f(m)$, where R

895   is the universal gas constant, ρ is the density of ice, S_{ice} is the ice saturation ratio ($S_{ice} = $

896     $RH_{ice}/100\%$), M_w is the water molecular weight, $\sigma_{i/v}$ is the surface tension at the ice-

897   vapor interface. $f(m)$ is the geometric factor and is defined as $f(m) = (m^3 - 3m + $

898     $2)/4$, where $m = \cos(\theta)$. A smaller value of θ implies higher ice nucleation efficiency

899   and should translate to relatively lower RH_{ice} onsets in our experiments. Figure 13

900   represents the mean θ as a function of temperature for INPs of all sample types. When

901   comparing θ at the same temperature, the FreshSS and AgedSS dominated samples, in

902   general, have the smallest θ, followed by the Dust dominated, CNOS and SS/Sulf

903   dominated, and BBA influenced samples. For all the investigated samples, θ was

904   relatively constant above 220 K and increased as temperature decreased to 205 K. We

905   propose new parameterizations of θ as a function of $T^3\ln[RH_{ice}]^2$ (Text S2). θ for

906   various particle types fall tightly into the parameterization as shown in Fig. S19.

907
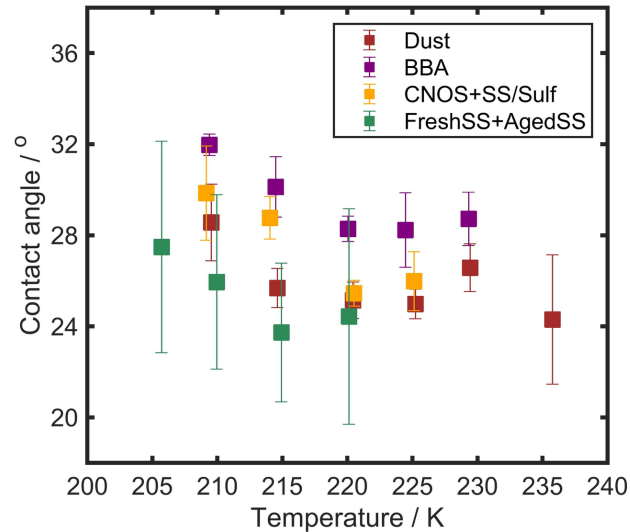
Figure 13. Mean values with one standard deviations of contact angle for DIN by the Dust, BBA,

909   CNOS and SS/Sulf, FreshSS and AgedSS dominated samples.

910

3.7 Ice nucleation propensity and mixing state of particle population

912   Previous studies have used χ to estimate the error in predicting aerosol CCN activity

913   and optical properties when assuming idealized mixing states (Ching et al., 2017; Yao

914   et al., 2022). For example, Ching et al. (2017) quantified the error in predicting CCN

915   concentration as a function of χ. When internal mixing was assumed, errors of up to

916   100% overpredicting CCN concentration were found for populations with more

917   external mixing ($\chi < 60\%$). However, CCN concentrations were well predicted for

918   populations with $\chi > 75\%$. Inspired by these studies, we used θ as a measure of particle

919   ice nucleation propensity to discuss the potential link between the mixed state of

920   population and particle ice nucleation propensity. We investigated the relative

921   difference (error) in θ for the field samples compared to pure NaCl particles. Ice

922   nucleation experiments were conducted on the laboratory-generated NaCl particles

923   (Text S3) and θ was calculated for NaCl particles (see Section 3.6.2 for the calculation

details). Pure NaCl particles were used as a surrogate of complete internally mixed marine aerosols ($\chi = 100\%$). We analyzed the relationship between the relative error in θ of INPs (*Err*) and the mixing state of the population in which the INPs were identified. *Err* of each INP from a field sample with a given mixing state (χ) was defined as:

$$Err = \frac{\theta(\chi) - \theta(100\%)}{\theta(100\%)} \times 100 \qquad (15)$$

where $\theta(100\%)$ is the average θ for the NaCl standard. As shown in Fig. 14, χ for the six investigated samples changed from 61% to 86%. Five samples (S1, S4, S10, S12, and S14) exhibited positive mean *Err* ranging from 2.3% ± 7.5% to 16.3% ± 6.6%, while S11 had a negative mean *Err* of -18.6% ± 6.2%. The FreshSS and AgedSS dominated samples, S4 and S12, have a mean *Err* of 6.9% ± 12.4% and 13.0% ± 9.2%, respectively.

The θ for particles in the marine environment is different from that for NaCl particles. This can lead to errors in J_{het} of several orders of magnitude if the model assumes an internally mixed particle population. According to CNT, we calculated DIN J_{het} for NaCl and particles with *Err* of 5% and 10% under different temperature and humidity conditions (Fig. S20). Between 135% and 180% RH_{ice}, *Err* of 5% and 10% will result in $1.5 - 4$ and $2 - 10$ orders of magnitude differences in J_{het}, respectively. Moreover, the lower the temperature and RH_{ice}, the larger the error in J_{het}. This suggests that the effects of aging processes and mixing state need to be considered in the ice nucleation modeling. No specific correlation or trend was found between χ and the *Err* from this data set with the limited number of samples. This may be expected since ice nucleation is controlled by various physiochemical properties of individual particles, particularly for DIN. For example, one crucial factor is the physical mixing state of particle, such as coating. Organic coatings play a significant role in altering the θ of sea salt particles, as exemplified by S11 compared to S4 and S12. In contrast to CCN, which in general can be described by the κ-Köhler theory, there are still no appropriate physical models to describe INPs. In addition, ice nucleation propensity for DIN is determined on the individual particle basis, whereas the chemical mixing state (i.e., χ here) characterizes

the overall mixing of species within the particle population. There is a large gap in the understanding of the relationship between INP propensity and χ.
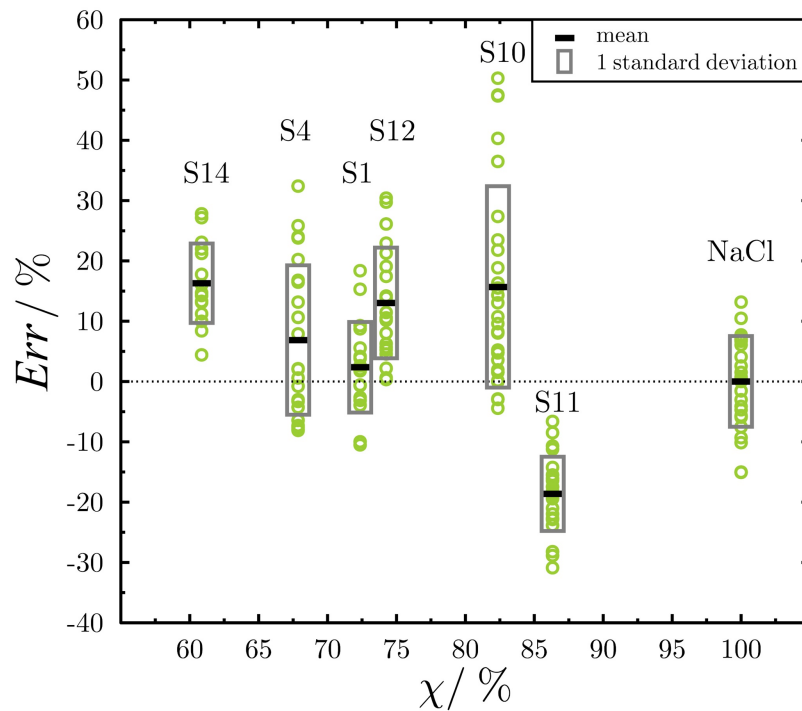
Figure 14. *Err* in θ for the investigated samples relative to the internally mixed particles (pure NaCl particles, χ = 100%). Black thick lines indicate the average θ and the gray boxes represent one standard deviation. Green circles represent θ for individual INPs.

4 Atmospheric implications

We found that the distinct mixing states of particle populations were affected by several processes over different oceans. In the marine atmosphere that already has a contribution of sea salt particles, adding more fresh sea salt particles makes the population more internally mixed (Fig. 6). We suspect that over open oceans where sea salt particle flux is large, the population will be mostly internally mixed. The addition of new particle types from other sources, such as dust storms (WP-I, S1, S2), biomass burning (WP-II, S14, S15), and secondary sources (CNOS in the SO region), will decrease the mixing state index and the population will become more externally mixed. These results are consistent with the proposed schematic description by Riemer et al. (2019) on the evolution of particle mixing state. We showed that multiphase processes

971 lead to the aging of fresh sea salt particles resulting in chlorine deficiency and thus

972 changing the mixing state of the population (Fig. 5). This is a selective process that

973 occurred on the sea salt particles and is different from the aging by condensation of

974 secondary materials. As discussed in Section 3.2, these types of selective or

975 inhomogeneous aging on particles move the population toward a more externally mixed

976 state. To the best of our knowledge, this is not considered in the models predicting the

977 mixing state of aerosols, even for the particle-resolved model. Our study suggests that,

978 when discussing the influence of aging on the evolution of the mixing state, it is

979 necessary to consider whether the aging processes occur uniformly on all particles.

980

981 We characterized chemical compositions for particle population and INPs at the single

982 particle level. We found that all the identified particle types from different sources have

983 the potential to serve as INPs, but have different ice nucleation efficiencies (Fig. 7 and

984 Fig. 9). We found that S11 showed the highest ice nucleation efficiency among the

985 FreshSS and AgedSS dominated samples (Fig. 7), which we attributed to the organic

986 coatings on the particles. This indicates the importance of characterizing the physical

987 mixing state of particles (i.e., morphology). INPs were enriched in SS/Sulf class,

988 suggesting that the aging process alters ice nucleation ability by changing the chemical

989 mixing state of particles. Considering the characterizations of individual particles and

990 INPs, the ice nucleation onset conditions, and the derived freezing kinetics, it is

991 suggested that the ice nucleation abilities at cirrus conditions of these complex marine

992 aerosols are affected not only by the particle compositions but also by the mixing state

993 of particle population. Future investigations on how the chemical and physical mixing

994 state of particles affects ice nucleation in the atmosphere are needed for a better

995 understanding of aerosol-cloud interactions in the climate system.

996

997 According to the singular hypothesis and CNT, ice nucleation kinetic parameters, J_{het}

998 and n_s, were derived from the experimental data. We derived parameterizations of n_s as

999 a function of temperature for IMF and DIN of different dominated particle classes. We

1000 also proposed parameterizations of J_{het} as a function of Δa_w for IMF and DIN based on

the water-activity based theory. In addition, θ was derived for DIN based on CNT. We propose new parameterizations of θ that take into account both temperature and RH_{ice}. These parameterizations can be used to estimate the INP concentrations or ice crystal production rates when particle surface area data are available. These parameterizations can be used in cloud models with different ice nucleation descriptions to evaluate the potential sources and impacts of different particles on cloud formation in the marine atmosphere.

5 Conclusions

Composition, mixing state, and ice nucleation properties were investigated for the aerosol particles collected over the Western Pacific and Southern Ocean during a cruise from South Korea (34.93°N) to the Ross Sea (75.12°S) in 2019. Seven particle classes were identified including fresh sea salt, aged sea salt, sea salt mixed with sulfate, carbonaceous particle, sulfur-containing particle, dust, and mixture. Contributions of these particles varied across oceans at different latitudes. Except for the samples impacted by dust storm, fresh sea salt, aged sea salt, and sea salt mixed with sulfate particles were the most prevalent particle types with the total number percentage ranging from 48% to 99%. Particles showed different degrees of chloride depletion due to the aging processes of acid displacements on sea salt particles. Significant contributions of sulfur-containing particles up to 93% in number were found in the Ross Sea, which was affected by phytoplankton blooms in the austral summer. The chemical mixing state index of particle population ranges from 50% to 95%. The mixing state index was positively correlated with the number percentages of fresh sea salt and negatively correlated with the proportion of sulfur-containing particles. Particle populations tended to be more internally mixed as the fresh sea salt fraction increased. When sea salt particles were a background or dominant particle type, inhomogeneous aging processes and new particle sources made the population more externally mixed.

We showed that different types of particle samples demonstrated a variety of ice

1030 nucleation abilities at cirrus conditions. The sample dominated by the fresh sea salt

1031 particles with organic coatings exhibited the highest ice nucleation efficiency with RH_{ice}

1032 onset as low as 121%, while particles influenced by biomass burning were the least

1033 efficient among the investigated samples. According to the individual INP

1034 characterizations, the dominant particle types in the population all contribute to the

1035 identified INPs but with different enrichment factors. The sea salt mixed with sulfate

1036 particles were enriched in INPs with an overall factor of about 1.9. Ice nucleation

1037 abilities of marine aerosol particles were affected not only by composition but also by

1038 the chemical and physical mixing state of the particle population. Ice nucleation kinetic

1039 parameters, time-dependent J_{het}, time-independent n_s, and contact angle, were derived

1040 from the experimental data. The corresponding parameterizations for different particle

1041 types are provided for cloud modeling. In this study, we demonstrated the diversity in

1042 the particle characteristics at the single particle level, the mixing state of particle

1043 population, and particles' abilities to form ice crystals in different marine atmospheres

1044 in both the northern and southern hemispheres. The results motivate the need for further

1045 investigations of how the mixing state of particles affects ice nucleation in the

1046 atmosphere.

1047

1048 **Data availability.** All data are given in the main text or in the Supplement. HYSPLIT

1049 data were obtained through the NOAA website (https://www.ready.noaa.gov/hypub-

1050 bin/trajasrc.pl). NAAPS aerosol reanalysis data were obtained from

1051 https://nrlgodae1.nrlmry.navy.mil/ftp/outgoing/nrl/NAAPS-REANALYSIS/. FIRMS

1052 data were obtained from https://firms.modaps.eosdis.nasa.gov/.

1053

1054 **Supplement.** The supplement related to this article is available online.

1055

1056 **Author contributions.** XJ performed the experiments and wrote the first draft of the

1057 manuscript. XJ, TZ, JP, and BW performed the data analysis. JP and KP collected

1058 the samples. BW, JP and KP initiated and designed the study. BW supervised the

project. BW, YJY, and XJ led the discussion and all authors contributed to the data interpretation and the manuscript writing.

Competing interests. The authors declare that they have no conflict of interest.

Acknowledgements. BW, XJ, and TZ thank the support by National Science Foundation of China (42075076, 41775133), Fundamental Research Funds for the Central Universities (20720160111, 20720190147). This study is also partially funded by the Korea Polar Research Institute research grant (PE23110, PE23030). BW and JY thank the support by the Fund of Key Laboratory of Global Change and Marine-Atmospheric Chemistry, MNR (GCMAC2004). TZ acknowledges the support by the PhD Fellowship of the State Key Laboratory of Marine Environmental Science at Xiamen University. We thank the staff onboard R/V *Araon* helping the sampling during the Antarctic cruise and Peter A. Alpert for helpful discussion and manuscript revision.

References

Adachi, K., Oshima, N., Gong, Z., de Sá, S., Bateman, A. P., Martin, S. T., de Brito, J. F., Artaxo, P., Cirino, G. G., Sedlacek III, A. J., and Buseck, P. R.: Mixing states of Amazon basin aerosol particles transported over long distances using transmission electron microscopy, Atmos. Chem. Phys., 20, 11923–11939, https://doi.org/10.5194/acp-20-11923-2020, 2020.

Alpert, P. A. and Knopf, D. A.: Analysis of isothermal and cooling-rate-dependent immersion freezing by a unifying stochastic ice nucleation model, Atmos. Chem. Phys., 16, 2083–2107, https://doi.org/10.5194/acp-16-2083-2016, 2016.

Alpert, P. A., Aller, J. Y., and Knopf, D. A.: Ice nucleation from aqueous NaCl droplets with and without marine diatoms, Atmos. Chem. Phys., 11, 5539–5555, https://doi.org/10.5194/acp-11-5539-2011, 2011a.

Alpert, P. A., Aller, J. Y., and Knopf, D. A.: Initiation of the ice phase by marine biogenic surfaces in supersaturated gas and supercooled aqueous phases, Phys. Chem. Chem. Phys., 13, 19882, https://doi.org/10.1039/c1cp21844a, 2011b.

Alpert, P. A., Kilthau, W. P., O'Brien, R. E., Moffet, R. C., Gilles, M. K., Wang, B., Laskin, A., Aller, J. Y., and Knopf, D. A.: Ice-nucleating agents in sea spray aerosol identified and quantified

1091 with a holistic multimodal freezing model, Sci. Adv., 8, 1–11,
1092 https://doi.org/10.1126/sciadv.abq6842, 2022.

1093 Angle, K. J., Crocker, D. R., Simpson, R. M. C., Mayer, K. J., Garofalo, L. A., Moore, A. N., Mora
1094 Garcia, S. L., Or, V. W., Srinivasan, S., Farhan, M., Sauer, J. S., Lee, C., Pothier, M. A., Farmer, D.
1095 K., Martz, T. R., Bertram, T. H., Cappa, C. D., Prather, K. A., and Grassian, V. H.: Acidity across
1096 the interface from the ocean surface to sea spray aerosol, Proc. Natl. Acad. Sci., 118, 1–6,
1097 https://doi.org/10.1073/pnas.2018397118, 2021.

1098 Ault, A. P., Moore, M. J., Furutani, H., and Prather, K. A.: Impact of emissions from the Los
1099 Angeles Port Region on San Diego air quality during regional transport events, Environ. Sci.
1100 Technol., 43, 3500–3506, https://doi.org/10/d7kt9s, 2009.

1101 Ault, A. P., Gaston, C. J., Wang, Y., Dominguez, G., Thiemens, M. H., and Prather, K. A.:
1102 Characterization of the single particle mixing state of individual ship plume events measured
1103 at the Port of Los Angeles, Environ. Sci. Technol., 44, 1954–1961,
1104 https://doi.org/10.1021/es902985h, 2010.

1105 Baccarini, A., Dommen, J., Lehtipalo, K., Henning, S., Modini, R. L., Gysel-Beer, M.,
1106 Baltensperger, U., and Schmale, J.: Low-volatility vapors and new particle formation over the
1107 Southern Ocean during the Antarctic circumnavigation expedition, J. Geophys. Res.: Atmos.,
1108 126, https://doi.org/10.1029/2021JD035126, 2021.

1109 Barnes, I., Hjorth, J., and Mihalopoulos, N.: Dimethyl sulfide and dimethyl sulfoxide and their
1110 oxidation in the atmosphere, Chem. Rev., 106, 940–975, https://doi.org/10.1021/cr020529+,
1111 2006.

1112 Beck, L. J., Sarnela, N., Junninen, H., Hoppe, C. J. M., Garmash, O., Bianchi, F., Riva, M., Rose,
1113 C., Peräkylä, O., Wimmer, D., Kausiala, O., Jokinen, T., Ahonen, L., Mikkilä, J., Hakala, J., He, X.,
1114 Kontkanen, J., Wolf, K. K. E., Cappelletti, D., Mazzola, M., Traversi, R., Petroselli, C., Viola, A. P.,
1115 Vitale, V., Lange, R., Massling, A., Nøjgaard, J. K., Krejci, R., Karlsson, L., Zieger, P., Jang, S., Lee,
1116 K., Vakkari, V., Lampilahti, J., Thakur, R. C., Leino, K., Kangasluoma, J., Duplissy, E., Siivola, E.,
1117 Marbouti, M., Tham, Y. J., Saiz-Lopez, A., Petäjä, T., Ehn, M., Worsnop, D. R., Skov, H., Kulmala,
1118 M., Kerminen, V., and Sipilä, M.: Differing mechanisms of new particle formation at two Arctic
1119 sites, Geophys. Res. Lett., 48, 1–11, https://doi.org/10/gjrb6h, 2021.

1120 Berndt, T., Hoffmann, E. H., Tilgner, A., Stratmann, F., and Herrmann, H.: Direct sulfuric acid
1121 formation from the gas-phase oxidation of reduced-sulfur compounds, Nat. Commun., 14,
1122 4849, https://doi.org/10/gs3whz, 2023.

1123 Brean, J., Dall' Osto, M., Simó, R., Shi, Z., Beddows, D. C. S., and Harrison, R. M.: Open ocean
1124 and coastal new particle formation from sulfuric acid and amines around the Antarctic
1125 Peninsula, Nat. Geosci., 14, 383–388, https://doi.org/10.1038/s41561-021-00751-y, 2021.

1126 Burrows, S. M., McCluskey, C. S., Cornwell, G., Steinke, I., Zhang, K., Zhao, B., Zawadowicz, M.,
1127 Raman, A., Kulkarni, G., China, S., Zelenyuk, A., and DeMott, P. J.: Ice-nucleating particles that

impact clouds and climate: observational and modeling research needs, Rev. Geophys., 60, 1–45, https://doi.org/10/gs6w5x, 2022.

Charnawskas, J. C., Alpert, P. A., Lambe, A. T., Berkemeier, T., O' Brien, R. E., Massoli, P., Onasch, T. B., Shiraiwa, M., Moffet, R. C., Gilles, M. K., Davidovits, P., Worsnop, D. R., and Knopf, D. A.: Condensed-phase biogenic-anthropogenic interactions with implications for cold cloud formation, Faraday Discuss., 200, 165–194, https://doi.org/10.1039/C7FD00010C, 2017.

Chen, J., Li, C., Ristovski, Z., Milic, A., Gu, Y., Islam, M. S., Wang, S., Hao, J., Zhang, H., He, C., Guo, H., Fu, H., Miljevic, B., Morawska, L., Thai, P., Lam, Y. F., Pereira, G., Ding, A., Huang, X., and Dumka, U. C.: A review of biomass burning: Emissions and impacts on air quality, health and climate in China, Sci. Total Environ., 579, 1000–1034, https://doi.org/10.1016/j.scitotenv.2016.11.025, 2017.

Chen, Q., Sherwen, T., Evans, M., and Alexander, B.: DMS oxidation and sulfur aerosol formation in the marine troposphere: a focus on reactive halogen and multiphase chemistry, Atmos. Chem. Phys., 18, 13617–13637, https://doi.org/10.5194/acp-18-13617-2018, 2018.

China, S., Alpert, P. A., Zhang, B., Schum, S., Dzepina, K., Wright, K., Owen, R. C., Fialho, P., Mazzoleni, L. R., Mazzoleni, C., and Knopf, D. A.: Ice cloud formation potential by free tropospheric particles from long-range transport over the Northern Atlantic Ocean, J. Geophys. Res.: Atmos., 122, 3065–3079, https://doi.org/10.1002/2016JD025817, 2017.

China, S., Burrows, S. M., Wang, B., Harder, T. H., Weis, J., Tanarhte, M., Rizzo, L. V., Brito, J., Cirino, G. G., Ma, P.-L., Cliff, J., Artaxo, P., Gilles, M. K., and Laskin, A.: Fungal spores as a source of sodium salt particles in the Amazon basin, Nat. Commun., 9, 4793, https://doi.org/10.1038/s41467-018-07066-4, 2018.

Ching, J., Fast, J., West, M., and Riemer, N.: Metrics to quantify the importance of mixing state for CCN activity, Atmos. Chem. Phys., 17, 7445–7458, https://doi.org/10.5194/acp-17-7445-2017, 2017.

Chou, C., Kanji, Z. A., Stetzer, O., Tritscher, T., Chirico, R., Heringa, M. F., Weingartner, E., Prévôt, A. S. H., Baltensperger, U., and Lohmann, U.: Effect of photochemical ageing on the ice nucleation properties of diesel and wood burning particles, Atmos. Chem. Phys., 13, 761–772, https://doi.org/10.5194/acp-13-761-2013, 2013.

Cochran, R. E., Ryder, O. S., Grassian, V. H., and Prather, K. A.: Sea spray aerosol: The chemical link between the oceans, atmosphere, and climate, Acc. Chem. Res., 50, 599–604, https://doi.org/10.1021/acs.accounts.6b00603, 2017.

Connolly, P. J., Möhler, O., Field, P. R., Saathoff, H., Burgess, R., Choularton, T., and Gallagher, M.: Studies of heterogeneous freezing by three different desert dust samples, Atmos. Chem. Phys., 9, 2805–2824, https://doi.org/10/bhhzwn, 2009.

Cornwell, G. C., McCluskey, C. S., Levin, E. J. T., Suski, K. J., DeMott, P. J., Kreidenweis, S. M., and Prather, K. A.: Direct online mass spectrometry measurements of ice nucleating particles

at a California coastal site, J. Geophys. Res.: Atmos., 124, 12157–12172, https://doi.org/10.1029/2019JD030466, 2019.

Cziczo, D. J., Ladino, L., Boose, Y., Kanji, Z. A., Kupiszewski, P., Lance, S., Mertes, S., and Wex, H.: Measurements of ice nucleating particles and ice residuals, Meteorol. Monogr., 58, 8.1-8.13, https://doi.org/10.1175/AMSMONOGRAPHS-D-16-0008.1, 2017.

De Leeuw, G., Andreas, E. L., Anguelova, M. D., Fairall, C. W., Lewis, E. R., O'Dowd, C., Schulz, M., and Schwartz, S. E.: Production flux of sea spray aerosol, Rev. Geophys., 49, 1–39, https://doi.org/10.1029/2010RG000349, 2011.

DeMott, P. J., Chen, Y., Kreidenweis, S. M., Rogers, D. C., and Sherman, D. E.: Ice formation by black carbon particles, Geophys. Res. Lett., 26, 2429–2432, https://doi.org/10.1029/1999GL900580, 1999.

DeMott, P. J., Petters, M. D., Prenni, A. J., Carrico, C. M., Kreidenweis, S. M., Collett, J. L., and Moosmüller, H.: Ice nucleation behavior of biomass combustion particles at cirrus temperatures, J. Geophys. Res.: Atmos., 114, 1–13, https://doi.org/10.1029/2009JD012036, 2009.

DeMott, P. J., Hill, T. C. J., McCluskey, C. S., Prather, K. A., Collins, D. B., Sullivan, R. C., Ruppel, M. J., Mason, R. H., Irish, V. E., Lee, T., Hwang, C. Y., Rhee, T. S., Snider, J. R., McMeeking, G. R., Dhaniyala, S., Lewis, E. R., Wentzell, J. J. B., Abbatt, J., Lee, C., Sultana, C. M., Ault, A. P., Axson, J. L., Diaz Martinez, M., Venero, I., Santos-Figueroa, G., Stokes, M. D., Deane, G. B., Mayol-Bracero, O. L., Grassian, V. H., Bertram, T. H., Bertram, A. K., Moffett, B. F., and Franc, G. D.: Sea spray aerosol as a unique source of ice nucleating particles, Proc. Natl. Acad. Sci. U.S.A., 113, 5797–5803, https://doi.org/10.1073/pnas.1514034112, 2016.

Ditas, J., Ma, N., Zhang, Y., Assmann, D., Neumaier, M., Riede, H., Karu, E., Williams, J., Scharffe, D., Wang, Q., Saturno, J., Schwarz, J. P., Katich, J. M., McMeeking, G. R., Zahn, A., Hermann, M., Brenninkmeijer, C. A. M., Andreae, M. O., Pöschl, U., Su, H., and Cheng, Y.: Strong impact of wildfires on the abundance and aging of black carbon in the lowermost stratosphere, Proc. Natl. Acad. Sci., 115, E11595–E11603, https://doi.org/10.1073/pnas.1806868115, 2018.

Ervens, B., Sorooshian, A., Aldhaif, A. M., Shingler, T., Crosbie, E., Ziemba, L., Campuzano-Jost, P., Jimenez, J. L., and Wisthaler, A.: Is there an aerosol signature of chemical cloud processing?, Atmos. Chem. Phys., 18, 16099–16119, https://doi.org/10.5194/acp-18-16099-2018, 2018.

Fraund, M., Pham, D., Bonanno, D., Harder, T., Wang, B., Brito, J., de Sá, S., Carbone, S., China, S., Artaxo, P., Martin, S., Pöhlker, C., Andreae, M., Laskin, A., Gilles, M., and Moffet, R.: Elemental mixing state of aerosol particles collected in central Amazonia during GoAmazon2014/15, Atmosphere, 8, 1–27, https://doi.org/10.3390/atmos8090173, 2017.

Fu, P. Q., Kawamura, K., Chen, J., Charrière, B., and Sempéré, R.: Organic molecular composition of marine aerosols over the Arctic Ocean in summer: Contributions of primary emission and secondary aerosol formation, Biogeosciences, 10, 653–667,

1202   https://doi.org/10.5194/bg-10-653-2013, 2013.

1203   Fuzzi, S., Decesari, S., Facchini, M. C., Cavalli, F., Emblico, L., Mircea, M., Andreae, M. O., Trebs,
1204   I., Hoffer, A., Guyon, P., Artaxo, P., Rizzo, L. V., Lara, L. L., Pauliquevis, T., Maenhaut, W., Raes,
1205   N., Chi, X., Mayol-Bracero, O. L., Soto-García, L. L., Claeys, M., Kourtchev, I., Rissler, J., Swietlicki,
1206   E., Tagliavini, E., Schkolnik, G., Falkovich, A. H., Rudich, Y., Fisch, G., and Gatti, L. V.: Overview
1207   of the inorganic and organic composition of size-segregated aerosol in Rondônia, Brazil, from
1208   the biomass-burning period to the onset of the wet season, J. Geophys. Res.: Atmos., 112, 1–
1209   35, https://doi.org/10.1029/2005JD006741, 2007.

1210   Geng, X., Zhong, G., Li, J., Cheng, Z., Mo, Y., Mao, S., Su, T., Jiang, H., Ni, K., and Zhang, G.:
1211   Molecular marker study of aerosols in the northern South China Sea: Impact of atmospheric
1212   outflow from the Indo-China Peninsula and South China, Atmos. Environ., 206, 225–236,
1213   https://doi.org/10.1016/j.atmosenv.2019.02.033, 2019.

1214   Han, Y., Fang, X., Xi, X., Song, L., and Yang, S.: Dust storm in Asia continent and its bio-
1215   environmental effects in the North Pacific: A case study of the strongest dust event in April,
1216   2001 in central Asia, Sci. Bull., 51, 723–730, https://doi.org/10.1007/s11434-006-0723-2,
1217   2006.

1218   Healy, R. M., Sciare, J., Poulain, L., Crippa, M., Wiedensohler, A., Prévôt, A. S. H., Baltensperger,
1219   U., Sarda-Estève, R., McGuire, M. L., Jeong, C.-H., McGillicuddy, E., O' Connor, I. P., Sodeau,
1220   J. R., Evans, G. J., and Wenger, J. C.: Quantitative determination of carbonaceous particle
1221   mixing state in Paris using single-particle mass spectrometer and aerosol mass spectrometer
1222   measurements, Atmos. Chem. Phys., 13, 9479–9496, https://doi.org/10.5194/acp-13-9479-
1223   2013, 2013.

1224   Hirsch, E. and Koren, I.: Record-breaking aerosol levels explained by smoke injection into the
1225   stratosphere, Science, 371, 1269–1274, https://doi.org/10.1126/science.abe1415, 2021.

1226   Hodshire, A. L., Akherati, A., Alvarado, M. J., Brown-Steiner, B., Jathar, S. H., Jimenez, J. L.,
1227   Kreidenweis, S. M., Lonsdale, C. R., Onasch, T. B., Ortega, A. M., and Pierce, J. R.: Aging effects
1228   on biomass burning aerosol mass and composition: a critical review of field and laboratory
1229   studies, Environ. Sci. Technol., 53, 10007–10022, https://doi.org/10.1021/acs.est.9b02588,
1230   2019.

1231   Hoose, C. and Möhler, O.: Heterogeneous ice nucleation on atmospheric aerosols: a review
1232   of results from laboratory experiments, Atmos. Chem. Phys., 12, 9817–9854,
1233   https://doi.org/10.5194/acp-12-9817-2012, 2012.

1234   Hopkins, R. J., Desyaterik, Y., Tivanski, A. V., Zaveri, R. A., Berkowitz, C. M., Tyliszczak, T., Gilles,
1235   M. K., and Laskin, A.: Chemical speciation of sulfur in marine cloud droplets and particles:
1236   Analysis of individual particles from the marine boundary layer over the California current, J.
1237   Geophys. Res.: Atmos., 113, 1–15, https://doi.org/10.1029/2007JD008954, 2008.

1238   Inoue, J., Tobo, Y., Taketani, F., and Sato, K.: Oceanic supply of ice-nucleating particles and its

effect on ice cloud formation: A case study in the Arctic Ocean during a cold-air outbreak in early winter, Geophys. Res. Lett., 48, https://doi.org/10.1029/2021GL094646, 2021.

IPCC: Climate Change 2013: The Physical Science Basis. Contribution of Working Group I to the Fifth Assessment Report of the Intergovernmental Panel on Climate Change, Cambridge University Press, Cambridge, United Kingdom and New York, NY, USA, 2013.

IPCC: Climate change 2021: the physical science basis, Cambridge University Press, 2021.

Jang, E., Park, K.-T., Yoon, Y. J., Kim, T.-W., Hong, S.-B., Becagli, S., Traversi, R., Kim, J., and Gim, Y.: New particle formation events observed at the King Sejong Station, Antarctic Peninsula – Part 2: Link with the oceanic biological activities, Atmos. Chem. Phys., 19, 7595–7608, https://doi.org/10.5194/acp-19-7595-2019, 2019.

Jang, J., Park, J., Park, J., Yoon, Y. J., Dall' Osto, M., Park, K.-T., Jang, E., Lee, J. Y., Cho, K. H., and Lee, B. Y.: Ocean-atmosphere interactions: Different organic components across Pacific and Southern Oceans, Sci. Total Environ., 878, 1–12, https://doi.org/10/gs3zkw, 2023.

Kanji, Z. A., DeMott, P. J., Möhler, O., and Abbatt, J. P. D.: Results from the University of Toronto continuous flow diffusion chamber at ICIS 2007: instrument intercomparison and ice onsets for different aerosol types, Atmos. Chem. Phys., 11, 31–41, https://doi.org/10.5194/acp-11-31-2011, 2011.

Kanji, Z. A., Ladino, L. A., Wex, H., Boose, Y., Burkert-Kohn, M., Cziczo, D. J., and Krämer, M.: Overview of ice nucleating particles, Meteorol. Monogr., 58, 1.1-1.33, https://doi.org/10.1175/AMSMONOGRAPHS-D-16-0006.1, 2017.

Khvorostyanov, V. I. and Curry, J. A.: The theory of ice nucleation by heterogeneous freezing of deliquescent mixed CCN. Part I: Critical radius, energy, and nucleation rate, J. Atmos. Sci., 61, 2676–2691, https://doi.org/10/b7nhwf, 2004.

Knopf, D. A. and Alpert, P. A.: A water activity based model of heterogeneous ice nucleation kinetics for freezing of water and aqueous solution droplets, Faraday Discuss., 165, 513–534, https://doi.org/10.1039/c3fd00035d, 2013.

Knopf, D. A., Alpert, P. A., Wang, B., and Aller, J. Y.: Stimulation of ice nucleation by marine diatoms, Nat. Geosci., 4, 88–90, https://doi.org/10.1038/ngeo1037, 2011.

Knopf, D. A., Alpert, P. A., Wang, B., O' Brien, R. E., Kelly, S. T., Laskin, A., Gilles, M. K., and Moffet, R. C.: Microspectroscopic imaging and characterization of individually identified ice nucleating particles from a case field study, J. Geophys. Res.: Atmos., 119, 10,365-10,381, https://doi.org/10.1002/2014JD021866, 2014.

Knopf, D. A., Alpert, P. A., and Wang, B.: The role of organic aerosol in atmospheric ice nucleation: a review, ACS Earth Space Chem., 2, 168–202, https://doi.org/10.1021/acsearthspacechem.7b00120, 2018.

Knopf, D. A., Charnawskas, J. C., Wang, P., Wong, B., Tomlin, J. M., Jankowski, K. A., Fraund, M., Veghte, D. P., China, S., Laskin, A., Moffet, R. C., Gilles, M. K., Aller, J. Y., Marcus, M. A., Raveh-Rubin, S., and Wang, J.: Micro-spectroscopic and freezing characterization of ice-nucleating particles collected in the marine boundary layer in the eastern North Atlantic, Atmos. Chem. Phys., 22, 5377–5398, https://doi.org/10.5194/acp-22-5377-2022, 2022.

Knopf, D. A., Wang, P., Wong, B., Tomlin, J. M., Veghte, D. P., Lata, N. N., China, S., Laskin, A., Moffet, R. C., Aller, J. Y., Marcus, M. A., and Wang, J.: Physicochemical characterization of free troposphere and marine boundary layer ice-nucleating particles collected by aircraft in the eastern North Atlantic, Atmos. Chem. Phys., 23, 8659–8681, https://doi.org/10.5194/acp-23-8659-2023, 2023.

Koehler, K. A., DeMott, P. J., Kreidenweis, S. M., Popovicheva, O. B., Petters, M. D., Carrico, C. M., Kireeva, E. D., Khokhlova, T. D., and Shonija, N. K.: Cloud condensation nuclei and ice nucleation activity of hydrophobic and hydrophilic soot particles, Phys. Chem. Chem. Phys., 11, 7906–7920, https://doi.org/10.1039/b905334b, 2009.

Koop, T. and Zobrist, B.: Parameterizations for ice nucleation in biological and atmospheric systems, Phys. Chem. Chem. Phys., 11, 10839, https://doi.org/10.1039/b914289d, 2009.

Koop, T., Luo, B., Tsias, A., and Peter, T.: Water activity as the determinant for homogeneous ice nucleation in aqueous solutions, Nature, 406, 611–614, https://doi.org/10.1038/35020537, 2000.

Kulkarni, G., Sanders, C., Zhang, K., Liu, X., and Zhao, C.: Ice nucleation of bare and sulfuric acid-coated mineral dust particles and implication for cloud properties: Ice formation on dust particles, J. Geophys. Res.: Atmos., 119, 9993–10011, https://doi.org/10.1002/2014JD021567, 2014.

Kunwar, B., Pokhrel, A., Niwai, T., and Kawamura, K.: Spatial and longitudinal distributions of total carbon, nitrogen and sulfur together with water-soluble major ions in marine aerosols collected from the Western Pacific and Southern Ocean, J. Geophys. Res.: Atmos., 128, 1–23, https://doi.org/10.1029/2022JD037874, 2023.

Laskin, A., Iedema, M. J., and Cowin, J. P.: Quantitative time-resolved monitoring of nitrate formation in sea salt particles using a CCSEM/EDX single particle analysis, Environ. Sci. Technol., 36, 4948–4955, https://doi.org/10.1021/es020551k, 2002.

Laskin, A., Cowin, J. P., and Iedema, M. J.: Analysis of individual environmental particles using modern methods of electron microscopy and X-ray microanalysis, J. Electron. Spectrosc. Relat. Phenom., 150, 260–274, https://doi.org/10.1016/j.elspec.2005.06.008, 2006.

Laskin, A., Moffet, R. C., Gilles, M. K., Fast, J. D., Zaveri, R. A., Wang, B., Nigge, P., and Shutthanandan, J.: Tropospheric chemistry of internally mixed sea salt and organic particles: Surprising reactivity of NaCl with weak organic acids, J. Geophys. Res.: Atmos., 117, 1–12, https://doi.org/10.1029/2012JD017743, 2012.

Lata, N. N., Zhang, B., Schum, S., Mazzoleni, L., Brimberry, R., Marcus, M. A., Cantrell, W. H., Fialho, P., Mazzoleni, C., and China, S.: Aerosol composition, mixing state, and phase state of free tropospheric particles and their role in ice cloud formation, ACS Earth Space Chem., 5, 3499–3510, https://doi.org/10.1021/acsearthspacechem.1c00315, 2021.

Liu, X. and Penner, J. E.: Ice nucleation parameterization for global models, Meteorologische Zeitschrift, 499–514, https://doi.org/10/b3b83s, 2005.

Liu, Y., Minofar, B., Desyaterik, Y., Dames, E., Zhu, Z., Cain, J. P., Hopkins, R. J., Gilles, M. K., Wang, H., Jungwirth, P., and Laskin, A.: Internal structure, hygroscopic and reactive properties of mixed sodium methanesulfonate-sodium chloride particles, Phys. Chem. Chem. Phys., 13, 11846–11857, https://doi.org/10.1039/c1cp20444k, 2011.

MacKay, D. J. C.: Information theory, inference, and learning algorithms, Cambridge University Press, Cambridge, 628 pp., 2003.

McCluskey, C. S., Ovadnevaite, J., Rinaldi, M., Atkinson, J., Belosi, F., Ceburnis, D., Marullo, S., Hill, T. C. J., Lohmann, U., Kanji, Z. A., O'Dowd, C., Kreidenweis, S. M., and DeMott, P. J.: Marine and terrestrial organic ice-nucleating particles in pristine marine to continentally influenced Northeast Atlantic air masses, J. Geophys. Res.: Atmos., 123, 6196–6212, https://doi.org/10/gpjrfh, 2018a.

McCluskey, C. S., Hill, T. C. J., Humphries, R. S., Rauker, A. M., Moreau, S., Strutton, P. G., Chambers, S. D., Williams, A. G., McRobert, I., Ward, J., Keywood, M. D., Harnwell, J., Ponsonby, W., Loh, Z. M., Krummel, P. B., Protat, A., Kreidenweis, S. M., and DeMott, P. J.: Observations of ice nucleating particles over Southern Ocean waters, Geophys. Res. Lett., 45, 11–989, https://doi.org/10.1029/2018GL079981, 2018b.

McCoy, I. L., Bretherton, C. S., Wood, R., Twohy, C. H., Gettelman, A., Bardeen, C. G., and Toohey, D. W.: Influences of recent particle formation on Southern Ocean aerosol variability and low cloud properties, Journal of Geophysical Research: Atmospheres, 126, e2020JD033529, https://doi.org/10.1029/2020JD033529, 2021.

Möhler, O., Büttner, S., Linke, C., Schnaiter, M., Saathoff, H., Stetzer, O., Wagner, R., Krämer, M., Mangold, A., Ebert, V., and Schurath, U.: Effect of sulfuric acid coating on heterogeneous ice nucleation by soot aerosol particles, J. Geophys. Res.: Atmos., 110, 1–12, https://doi.org/10.1029/2004JD005169, 2005a.

Möhler, O., Linke, C., Saathoff, H., Schnaiter, M., Wagner, R., Mangold, A., Krämer, M., and Schurath, U.: Ice nucleation on flame soot aerosol of different organic carbon content, Meteorol. Zeitschrift, 14, 477–484, https://doi.org/10.1127/0941-2948/2005/0055, 2005b.

Murray, B. J., O'Sullivan, D., Atkinson, J. D., and Webb, M. E.: Ice nucleation by particles immersed in supercooled cloud droplets, Chem. Soc. Rev., 41, 6519–6554, https://doi.org/10.1039/c2cs35200a, 2012.

Myriokefalitakis, S., Vignati, E., Tsigaridis, K., Papadimas, C., Sciare, J., Mihalopoulos, N.,

1348 Facchini, M. C., Rinaldi, M., Dentener, F. J., Ceburnis, D., Hatzianastasiou, N., O' Dowd, C. D.,
1349 van Weele, M., and Kanakidou, M.: Global modeling of the oceanic source of organic aerosols,
1350 Adv. Meteorol., 2010, 1–16, https://doi.org/10.1155/2010/939171, 2010.

1351 Niemand, M., Möhler, O., Vogel, B., Vogel, H., Hoose, C., Connolly, P., Klein, H., Bingemer, H.,
1352 DeMott, P., Skrotzki, J., and Leisner, T.: A particle-surface-area-based parameterization of
1353 immersion freezing on desert dust particles, J. Atmos. Sci., 69, 3077–3092,
1354 https://doi.org/10/f4bkkr, 2012.

1355 O' Brien, R. E., Wang, B., Laskin, A., Riemer, N., West, M., Zhang, Q., Sun, Y., Yu, X., Alpert, P.,
1356 Knopf, D. A., Gilles, M. K., and Moffet, R. C.: Chemical imaging of ambient aerosol particles:
1357 Observational constraints on mixing state parameterization, J. Geophys. Res.: Atmos., 120,
1358 9591–9605, https://doi.org/10.1002/2015JD023480, 2015.

1359 Palm, B. B., Peng, Q., Fredrickson, C. D., Lee, B. H., Garofalo, L. A., Pothier, M. A., Kreidenweis,
1360 S. M., Farmer, D. K., Pokhrel, R. P., Shen, Y., Murphy, S. M., Permar, W., Hu, L., Campos, T. L.,
1361 Hall, S. R., Ullmann, K., Zhang, X., Flocke, F., Fischer, E. V., and Thornton, J. A.: Quantification
1362 of organic aerosol and brown carbon evolution in fresh wildfire plumes, Proc. Natl. Acad. Sci.
1363 U.S.A., 117, 29469–29477, https://doi.org/10.1073/pnas.2012218117, 2020.

1364 Park, J., Dall' Osto, M., Park, K., Gim, Y., Kang, H. J., Jang, E., Park, K.-T., Park, M., Yum, S. S.,
1365 Jung, J., Lee, B. Y., and Yoon, Y. J.: Shipborne observations reveal contrasting Arctic marine,
1366 Arctic terrestrial and Pacific marine aerosol properties, Atmos. Chem. Phys., 20, 5573–5590,
1367 https://doi.org/10.5194/acp-20-5573-2020, 2020.

1368 Park, J. Y., Lim, S., and Park, K.: Mixing state of submicrometer sea spray particles enriched by
1369 insoluble species in bubble-bursting experiments, J. Atmos. Ocean. Technol., 31, 93–104,
1370 https://doi.org/10.1175/JTECH-D-13-00086.1, 2014.

1371 Primm, K. M., Schill, G. P., Veghte, D. P., Freedman, M. A., and Tolbert, M. A.: Depositional ice
1372 nucleation on NX illite and mixtures of NX illite with organic acids, J. Atmos. Chem., 74, 55–
1373 69, https://doi.org/10.1007/s10874-016-9340-x, 2017.

1374 Pruppacher, H. R. and Klett, J. D.: Microphysics of clouds and precipitation, Springer
1375 Netherlands, Dordrecht, 954 pp., https://doi.org/10.1007/978-0-306-48100-0, 2010.

1376 Riemer, N. and West, M.: Quantifying aerosol mixing state with entropy and diversity
1377 measures, Atmos. Chem. Phys., 13, 11423–11439, https://doi.org/10.5194/acp-13-11423-
1378 2013, 2013.

1379 Riemer, N., Ault, A. P., West, M., Craig, R. L., and Curtis, J. H.: Aerosol mixing state:
1380 measurements, modeling, and impacts, Rev. Geophys., 57, 187–249,
1381 https://doi.org/10.1029/2018RG000615, 2019.

1382 Rolph, G., Stein, A., and Stunder, B.: Real-time environmental applications and display system:
1383 ready, Environ. Model Softw., 95, 210–228, https://doi.org/10.1016/j.envsoft.2017.06.025,
1384 2017.

Schill, G. P. and Tolbert, M. A.: Heterogeneous ice nucleation on simulated sea-spray aerosol using Raman microscopy, J. Phys. Chem. C, 118, 29234–29241, https://doi.org/10.1021/jp505379j, 2014.

Song, Y., Qiao, F., Liu, J., Shu, Q., Bao, Y., Wei, M., and Song, Z.: Effects of sea spray on large-scale climatic features over the Southern Ocean, J. Clim., 35, 4645–4663, https://doi.org/10.1175/JCLI-D-21-0608.1, 2022.

Stein, A. F., Draxler, R. R., Rolph, G. D., Stunder, B. J. B., Cohen, M. D., and Ngan, F.: NOAA's HYSPLIT atmospheric transport and dispersion modeling system, Bull. Am. Meteorol. Soc., 96, 2059–2077, https://doi.org/10.1175/BAMS-D-14-00110.1, 2015.

Su, B., Wang, T., Zhang, G., Liang, Y., Lv, C., Hu, Y., Li, L., Zhou, Z., Wang, X., and Bi, X.: A review of atmospheric aging of sea spray aerosols: Potential factors affecting chloride depletion, Atmos. Environ., 290, 1–24, https://doi.org/10.1016/j.atmosenv.2022.119365, 2022.

Tang, M., Cziczo, D. J., and Grassian, V. H.: Interactions of water with mineral dust aerosol: water adsorption, hygroscopicity, cloud condensation, and ice nucleation, Chem. Rev., 116, 4205–4259, https://doi.org/10.1021/acs.chemrev.5b00529, 2016.

Tang, M. J., Schuster, G., and Crowley, J. N.: Heterogeneous reaction of N_2O_5 with illite and Arizona test dust particles, Atmos. Chem. Phys., 14, 245–254, https://doi.org/10.5194/acp-14-245-2014, 2014.

Tomlin, J. M., Jankowski, K. A., Veghte, D. P., China, S., Wang, P., Fraund, M., Weis, J., Zheng, G., Wang, Y., Rivera-Adorno, F., Raveh-Rubin, S., Knopf, D. A., Wang, J., Gilles, M. K., Moffet, R. C., and Laskin, A.: Impact of dry intrusion events on the composition and mixing state of particles during the winter Aerosol and Cloud Experiment in the Eastern North Atlantic (ACE-ENA), Atmos. Chem. Phys., 21, 18123–18146, https://doi.org/10.5194/acp-21-18123-2021, 2021.

Tomlin, J. M., Weis, J., Veghte, D. P., China, S., Fraund, M., He, Q., Reicher, N., Li, C., Jankowski, K. A., Rivera-Adorno, F. A., Morales, A. C., Rudich, Y., Moffet, R. C., Gilles, M. K., and Laskin, A.: Chemical composition and morphological analysis of atmospheric particles from an intensive bonfire burning festival, Environ. Sci.: Atmos., 2, 616–633, https://doi.org/10.1039/D2EA00037G, 2022.

Vali, G.: Qauantitative evaluation of experimental results on the heterogeneous freezing nucleation of supercooled liquids, J. Atmos. Sci., 28, 402–409, https://doi.org/10.1175/1520-0469(1971)028<0402:QEOERA>2.0.CO;2, 1971.

Wagner, R., Kaufmann, J., Möhler, O., Saathoff, H., Schnaiter, M., Ullrich, R., and Leisner, T.: Heterogeneous ice nucleation ability of NaCl and sea salt aerosol particles at cirrus temperatures, J. Geophys. Res.: Atmos., 123, 2841–2860, https://doi.org/10.1002/2017JD027864, 2018.

Wang, B. and Knopf, D. A.: Heterogeneous ice nucleation on particles composed of humic-

1422 like substances impacted by O_3, J. Geophys. Res.: Atmos., 116, 1–14,
1423 https://doi.org/10.1029/2010JD014964, 2011.

1424 Wang, B., Laskin, A., Roedel, T., Gilles, M. K., Moffet, R. C., Tivanski, A. V., and Knopf, D. A.:
1425 Heterogeneous ice nucleation and water uptake by field-collected atmospheric particles
1426 below 273 K, J. Geophys. Res.: Atmos., 117, 1–15, https://doi.org/10.1029/2012JD017446,
1427 2012a.

1428 Wang, B., Lambe, A. T., Massoli, P., Onasch, T. B., Davidovits, P., Worsnop, D. R., and Knopf, D.
1429 A.: The deposition ice nucleation and immersion freezing potential of amorphous secondary
1430 organic aerosol: Pathways for ice and mixed-phase cloud formation, J. Geophys. Res.: Atmos.,
1431 117, 1–12, https://doi.org/10.1029/2012JD018063, 2012b.

1432 Wang, B., O' Brien, R. E., Kelly, S. T., Shilling, J. E., Moffet, R. C., Gilles, M. K., and Laskin, A.:
1433 Reactivity of liquid and semisolid secondary organic carbon with chloride and nitrate in
1434 atmospheric aerosols, J. Phys. Chem. A, 119, 4498–4508, https://doi.org/10.1021/jp510336q,
1435 2015.

1436 Wang, B., Harder, T. H., Kelly, S. T., Piens, D. S., China, S., Kovarik, L., Keiluweit, M., Arey, B. W.,
1437 Gilles, M. K., and Laskin, A.: Airborne soil organic particles generated by precipitation, Nat.
1438 Geosci., 9, 433–437, https://doi.org/10.1038/ngeo2705, 2016a.

1439 Wang, B., Knopf, D. A., China, S., Arey, B. W., Harder, T. H., Gilles, M. K., and Laskin, A.: Direct
1440 observation of ice nucleation events on individual atmospheric particles, Phys. Chem. Chem.
1441 Phys., 18, 29721–29731, https://doi.org/10.1039/C6CP05253C, 2016b.

1442 Welti, A., Lüönd, F., Stetzer, O., and Lohmann, U.: Influence of particle size on the ice
1443 nucleating ability of mineral dusts, Atmos. Chem. Phys., 9, 6705–6715,
1444 https://doi.org/10.5194/acp-9-6705-2009, 2009.

1445 Welti, A., Bigg, E. K., DeMott, P. J., Gong, X., Hartmann, M., Harvey, M., Henning, S., Herenz,
1446 P., Hill, T. C. J., Hornblow, B., Leck, C., Löffler, M., McCluskey, C. S., Rauker, A. M., Schmale, J.,
1447 Tatzelt, C., van Pinxteren, M., and Stratmann, F.: Ship-based measurements of ice nuclei
1448 concentrations over the Arctic, Atlantic, Pacific and Southern oceans, Atmos. Chem. Phys., 20,
1449 15191–15206, https://doi.org/10.5194/acp-20-15191-2020, 2020.

1450 Wilson, T. W., Ladino, L. A., Alpert, P. A., Breckels, M. N., Brooks, I. M., Browse, J., Burrows, S.
1451 M., Carslaw, K. S., Huffman, J. A., Judd, C., Kilthau, W. P., Mason, R. H., McFiggans, G., Miller,
1452 L. A., Nájera, J. J., Polishchuk, E., Rae, S., Schiller, C. L., Si, M., Temprado, J. V., Whale, T. F.,
1453 Wong, J. P. S., Wurl, O., Yakobi-Hancock, J. D., Abbatt, J. P. D., Aller, J. Y., Bertram, A. K., Knopf,
1454 D. A., and Murray, B. J.: A marine biogenic source of atmospheric ice-nucleating particles,
1455 Nature, 525, 234–238, https://doi.org/10.1038/nature14986, 2015.

1456 Xiao, H. S., Dong, J. L., Wang, L. Y., Zhao, L. J., Wang, F., and Zhang, Y. H.: Spatially resolved
1457 micro-Raman observation on the phase separation of effloresced sea salt droplets, Environ.
1458 Sci. Technol., 42, 8698–8702, https://doi.org/10.1021/es801181f, 2008.

1459   Yakobi-Hancock, J. D., Ladino, L. A., and Abbatt, J. P. D.: Feldspar minerals as efficient
1460   deposition ice nuclei, Atmos. Chem. Phys., 13, 11175–11185, https://doi.org/10.5194/acp-13-
1461   11175-2013, 2013.

1462   Yan, J., Jung, J., Zhang, M., Bianchi, F., Tham, Y. J., Xu, S., Lin, Q., Zhao, S., Li, L., and Chen, L.:
1463   Uptake selectivity of methanesulfonic acid (MSA) on fine particles over polynya regions of the
1464   Ross Sea, Antarctica, Atmos. Chem. Phys., 20, 3259–3271, https://doi.org/10.5194/acp-20-
1465   3259-2020, 2020.

1466   Yao, Y., Curtis, J. H., Ching, J., Zheng, Z., and Riemer, N.: Quantifying the effects of mixing state
1467   on aerosol optical properties, Atmos. Chem. Phys., 22, 9265–9282, https://doi.org/10/gr2nbf,
1468   2022.

1469   Zhang, M., Chen, L., Xu, G., Lin, Q., and Liang, M.: Linking phytoplankton activity in polynyas
1470   and sulfur aerosols over Zhongshan Station, East Antarctica, J. Atmos. Sci., 72, 4629–4642,
1471   https://doi.org/10.1175/JAS-D-15-0094.1, 2015.

1472